

The EUMETSAT  
Network of  
Satellite  
Application  
Facilities



**ROM SAF**

Radio Occultation Meteorology

## **ROM SAF CDOP-2**

### **Visiting Scientist Report 26:**

#### **Characterisation of radiosonde temperature biases and errors using radio occultation measurements**

**Jordis S. Tradowsky**

Danish Meteorological Institute (DMI)  
European Centre for Medium-Range Weather Forecasts (ECMWF)  
Institut d'Estudis Espacials de Catalunya (IEEC)  
Met Office (METO)

## DOCUMENT AUTHOR TABLE

	<b>Author(s)</b>	<b>Function</b>	<b>Date</b>	<b>Comment</b>
Prepared by:	Jordis Tradowsky	ROM SAF Visiting Scientist	4/07/2015	
Reviewed by (Internal):	Chris Burrows	ROM SAF Project Team	06/11/2015	
Reviewed by (Internal):	Sean Healy	ROM SAF Local Manager	16/11/2015	
Reviewed by:	Axel von Engel'n	Remote Sensing Scientist	23/11/2015	EUMETSAT
Approved by:	Kent B. Lauritsen	ROM SAF Project Manager	07/07/2016	

## DOCUMENT CHANGE RECORD

<b>Issue/Revision</b>	<b>Date</b>	<b>By</b>	<b>Description</b>
Version 0.1	30th October 2015	JT	First version
Version 0.2	10th November 2015	CB	Added comments
Version 0.3	16th November 2015	JT	Updated with Sean Healy's comments
Version 0.4	30th November 2015	JT	Updated with Axel von Engel'n's comments
Version 1.0	2nd December 2015	JT	Final version
Version 1.1	8th January 2016	JT	Minor changes to version 1.0
Version 1.2	4th July 2016	JT	Updated figure 4.7. Updated some of the text to improve the writing and include more detail/knowledge that was generated in the ongoing research. Updated radiosonde type table. Prepared a supplementary document containing the statistics for all analysed upper-air sites. A paper with the title "A new method to correct radiosonde temperature biases using radio occultation data" is submitted to the AMS Journal of Applied Meteorology and Climate. The focus of the papers is describing the method applied in this ROM SAF VS26 report.

### VS Authors

This VS study was carried out by Jordis Tradowsky, Bodeker Scientific, New Zealand; email: jordistradowsky@gmail.com

### VS Duration

The VS study was performed during September - October 2015 at the Met Office with one short visit to ECMWF.

## **ROM SAF**

The Radio Occultation Meteorology Satellite Application Facility (ROM SAF) is a decentralised processing center under EUMETSAT which is responsible for operational processing of GRAS radio occultation data from the Metop satellites and Radio Occultation (RO) data from other missions. The ROM SAF delivers bending angle, refractivity, temperature, pressure, and humidity profiles in near-real time and offline for NWP and climate users. The offline profiles are further processed into climate products consisting of gridded monthly zonal means of bending angle, refractivity, temperature, humidity, and geopotential heights together with error descriptions.

The ROM SAF also maintains the Radio Occultation Processing Package (ROPP) which contains software modules that will aid users wishing to process, quality-control and assimilate radio occultation data from any radio occultation mission into NWP and other models.

The ROM SAF Leading Entity is the Danish Meteorological Institute (DMI), with Cooperating Entities: i) European Centre for Medium-Range Weather Forecasts (ECMWF) in Reading, United Kingdom, ii) Institut D'Estudis Espacials de Catalunya (IEEC) in Barcelona, Spain, and iii) Met Office in Exeter, United Kingdom. To get access to our products or to read more about the ROM SAF please go to: <http://www.romsaf.org>.

## **Intellectual Property Rights**

All intellectual property rights of the ROM SAF products belong to EUMETSAT. The use of these products is granted to every interested user, free of charge. If you wish to use these products, EUMETSAT's copyright credit must be shown by displaying the words "copyright (year) EUMETSAT" on each of the products used.

# List of Contents

<b>Executive Summary</b>	<b>5</b>
<b>1 Introduction</b>	<b>7</b>
<b>2 Method</b>	<b>9</b>
2.1 Linear Abel transform . . . . .	10
2.1.1 The tangent linear Abel transform . . . . .	11
2.2 Tdry calculation . . . . .	12
2.2.1 Hydrostatic integration . . . . .	12
2.3 Performance of the dry temperature calculation . . . . .	14
<b>3 Data and Model</b>	<b>16</b>
3.1 Radio occultation data . . . . .	16
3.1.1 Quality control RO . . . . .	16
3.1.2 The RO temperature null-space . . . . .	17
3.2 Radiosonde data . . . . .	17
3.2.1 Quality control RS . . . . .	18
3.3 Model . . . . .	18
<b>4 Sensitivity study</b>	<b>20</b>
4.1 Determining the lowest dry level . . . . .	20
4.2 Upper cut-off criterion for RO bending angles . . . . .	21
4.2.1 Influence of the linearisation state . . . . .	24
4.2.2 Covariance matrices for different upper cut-off impact heights . . . . .	24
4.2.3 Dependence on the highest level bending angle . . . . .	29
4.3 Radius around RS upper-air site . . . . .	31
4.4 Rising and setting occultations . . . . .	35
4.5 Solar elevation angle . . . . .	37
4.5.1 Radio occultation . . . . .	37
4.5.2 Radiosonde . . . . .	38
4.6 Different RO missions . . . . .	39
<b>5 Comparison of departure statistics for RS and RO</b>	<b>41</b>
<b>6 Conclusions</b>	<b>48</b>
6.1 Acknowledgements . . . . .	51
<b>Bibliography</b>	<b>52</b>
<b>A Acronyms and abbreviations</b>	<b>55</b>
<b>B Radiosonde types</b>	<b>56</b>

## Executive Summary

Measurements of atmospheric temperature have been made for decades and nowadays radiosonde (RS) and radio occultation (RO) measurements are used to anchor the temperature in numerical weather prediction (NWP) models. However, the impact of the high quality RO data might be limited due to opposing biases between the observation types. Therefore, for better exploitation of highly accurate RO measurements an improved bias correction in RS temperatures is needed. Here we use a new method to calculate the RS temperature bias on a station-by-station basis for different solar elevation angle ranges. The temperature bias corrections are calculated using fields from the Met Office Unified Model as a transfer medium. Thus the bias correction is calculated based on the background departure statistics, i.e. the difference between the measurement and the model background (short-range forecast). This method has two advantages: (i) compared to direct observation-to-observation co-locations, the influence of differences in time and space is minimized since every measurement (both RO and RS) has a co-located model background profile, and (ii) the lowest level where the calculated model dry temperature ( $T_{dry}$ ) is acceptably close to the model temperature, i.e. where the atmosphere is approximately dry, is determined for each profile, which allows the RO  $T_{dry}$  profiles to be used as low as is reasonable.

For this investigation the RO departure statistics are first calculated in bending angle (BA) space and are then propagated to  $T_{dry}$  departures using tangent linear versions of the linear Abel transform to obtain refractivity departures, and the hydrostatic integration of the refractivity to obtain  $T_{dry}$  departures. This method was suggested by Sean Healy (personal communication) and is, for the first time described here in detail. Using the tangent linear version of the  $T_{dry}$  calculation enables us to select the maximum impact height at which the RO BA departures are used, while the full non-linear version would not allow this flexibility. Choosing this upper limit above which the BA departures are set to zero is a crucial decision, since it influences the results. Since radiosondes only reach pressure levels of about 10 hPa, the aim is to use the minimum amount of data above 10 hPa in order to eliminate the effect of model biases at higher levels.

The results of this project show that the RS temperature bias varies from station-to-station. The temperature bias depends inter alia on the RS type, the correction software of the vendor and the position of the sun. While the calculated bias correction stays below 0.5 - 1 K for sites launching e.g. the Finish Vaisala RS92, the biases at other stations can be considerably higher. For most stations the bias increases with the altitude and reaches its maximum at 10 hPa, which is the lowest analysed pressure level. For some Russian sites biases of 2-3 K occur at the higher level in the atmosphere. Interestingly the Russian sondes tend to have a cold bias at higher levels for all solar elevation angles (SEAs). In contrast the Vaisala RS92, which is known as one of the most accurate radiosondes, tend to have a slight cold bias at the lower levels and a slight warm bias at the highest levels for high SEAs. RS92s launched at night tend to have a slight cold bias at most altitudes.

The large temperature biases found at some stations show the importance of applying an up-to-date bias correction to the RS temperature profiles before they are assimilated into NWP models. Thus opposing biases in RO and RS measurements can be minimised.

The results are intended to be used in a forecast impact study and could afterwards be implemented into operational weather forecast systems, where they would need to be updated on

a regular basis.

# 1 Introduction

This document contains the results from the ROM SAF Visiting Scientist activity on the characterisation of radiosonde (RS) temperature biases using radio occultation (RO) measurements. Radiosondes are launched daily from hundreds of upper-air sites worldwide and measure profiles of temperature, humidity and possibly pressure from the ground up to 30-40 km altitude. The RO technique (see e.g. Kursinski et al. [18]) allows the retrieval of atmospheric parameters, i.e. the Tdry, from signals of the Global Navigation Satellite System (GNSS).

For decades, RS profiles have been assimilated into NWP systems and since around 2006, RO data have been assimilated, demonstrating a positive impact on the weather forecasts (see e.g. Poli et al. [24], Rennie [26]). However, the impact of the high quality RO data might be limited due to opposing biases between the observation types. Furthermore, regional variations in temperature bias due to different RS characteristics may have the potential to cause false horizontal temperature gradients in the analyses, which may lead to errors in the wind field due to geostrophic adjustments. More crucially though, satellite radiance measurements require bias corrections, and these are computed relative to the model background or analysis (either statically or via variational methods). This can only be done consistently if sufficient "anchor" measurements are present in the assimilation system. Amongst these, RO and RS are key contributors, so ensuring consistency between the bias characteristics of these observations types is important for the stability of assimilation systems.

Therefore, to ensure the consistency between RS and RO measurements, this study provides a method to correct RS temperature bias on a station-by-station basis, where the biases are computed on RS standard pressure levels. The RO variable used here is the bending angle (BA) as a function of impact parameter, but some assumptions (see chapter 2) allow the retrieval of Tdry profiles which can be used in the absence of water vapour. In contrast to other studies which analyse the difference between RS and RO profiles based on spatial and temporal co-locations (see e.g. Sun et al. [32]), this investigation uses short-range global forecast (i.e. "background") fields from the Met Office Unified Model as transfer medium; we calculate the background departures (observation minus model background, O-B) for RO and RS respectively and compare the two sets of O-B statistics. The BA background fields are computed from the model fields with a forward model as described in Healy and Thépaut [13] and Burrows et al. [3].

This method has three advantages: (i) compared to direct observation-to-observation co-locations, the influence of differences in time and space are minimized, since every measurement (both RO and RS) has a co-located model background profile, i.e. the model is interpolated to the position and time of each measurement, (ii) the lowest level at which the model humidity is negligible can be determined for each RO profile, which allows the retrieved Tdry profiles to be used as low as is reasonable, and (iii) a tangent linear (TL) retrieval can be used. The knowledge of atmospheric humidity facilitates the investigation of the RS bias using Tdry from 10 hPa down to a location-dependent pressure level of about 100 hPa in the tropics and 300-400 hPa in the high latitudes [see also 19], which is generally lower than in other studies. For example, Sun et al. [32] use Tdry down to 150 hPa globally and wet temperature retrievals including *a priori* knowledge from the National Centers for Environmental Prediction 12 hour forecasts further down in the atmosphere. To avoid includ-

ing *a priori* knowledge about the humidity, we calculate the bias corrections only at heights for which water vapour effects are negligible. The bias calculated for the lowest levels might not be representative for all atmospheric conditions, but rather represent a sub-sample for especially dry conditions. For operational use in NWP systems a gradual transition of the bias corrections below these heights must be applied to avoid discontinuities in the assimilated temperature profiles.

The results from this report are intended to provide the basis for a forecast impact study, where the bias corrections will be applied to each station separately, with no Hawson correction used (Hawson and Caton [9]). Based on the outcome of the impact study, the results can possibly be implemented into the Met Office global data assimilation system. The results of temperature biases for each RS station, as presented here, may also be useful to the wider community. Since the bias is calculated on a station-by-station basis rather than by RS type, the bias correction will need to be updated regularly to account for changes in the RS types being used by each station and the calibration procedure. Operationally, this could be done monthly, using a weighted average of the inferred biases, where the weight decreases going further into the past. In this study the RS biases was calculated for the whole of 2014, where some of the bias corrections might be outdated by now, thus we mainly aim to present the technique and only show example biases for five stations. To perform this study some pragmatic choices were needed and therefore sensitivity tests were performed to decide the final set-up of the investigation.

This report begins by explaining the novel method applied here in chapter 2, continues by describing the RS and RO data sets in chapter 3, followed by various sensitivity studies (chapter 4) before the results are described in chapter 5. Finally, the implications of this investigation are discussed in chapter 6.

## 2 Method

The analysis of RS temperature biases is performed on a station-by-station basis, giving a vertical bias correction profile for each of the 762 studied sites ('site' and 'station' are used synonymously). In this report a carefully chosen subset of 5 sites comprising different climate regimes and different sonde types is presented. The bias profiles extend from 10 hPa to at least 100 hPa, and for most of the non-tropical stations, considerably lower into the atmosphere, a boundary which is determined by the humidity in the model atmosphere. Since the bias corrections at the lowest levels are calculated from a subset of RO profiles measured in an especially dry air masses, these bias corrections might not be representative for all atmospheric conditions.

Most of those upper-air stations that (i) submitted timely RS TEMP profiles to the Global Telecommunication System (GTS) in 2014 and (ii) launched at least 15 RS in one month of the year 2014 are analysed (i.e. ignoring launches from ships etc.). For each upper-air site, the RO BA profiles in a circle with a chosen radius around the site are selected using the haversine equation for the great circle distance and (i) the mean RO BA profile, (ii) the mean model BA profile and (iii) the mean BA departure (RO O-B) profile is calculated. Thus, instead of using only those RS and RO profiles that are closely co-located in time and space, all occultations within a given distance from the site, and all RS launched at the site, independent of the sonde type, are analysed. To calculate RS temperature biases using RO measurements, the BA departures need to be propagated to Tdry departures, so that equivalent quantities may be compared. First, the linear Abel transform is used to obtain inferred refractivity departures, and second, a hydrostatic integration of the refractivities is used to obtain Tdry departures as described in sections 2.1, 2.1.1 and 2.2.

Since the RS temperature biases are highly dependent on the position of the sun due to radiation effects, and RO profiles also show a slight dependence on the solar elevation angle (SEA) (see Healy and Culverwell [12]), both data sets are subdivided based on the SEA as described in section 4.5. Dividing into SEA ranges also takes into account some of the differences caused by the seasonal variability, which will not be regarded separately, because dividing the data based on the season would further decrease the sample size and reduce the statistical significance of the results. The mean RS temperature departure profile for each SEA range is compared with the mean RO Tdry departures for the same SEA range. With this technique a bias correction can be performed from 10 hPa down to the lowest level where a sufficient amount of dry RO temperature profiles is available. To test if the humidity in atmosphere is low enough to use the RO Tdry, the model humidity is analysed as described in section 4.1.

The use of O-B statistics for both observation types minimizes effects caused by spatial and temporal co-location errors, and hence statistical significance is improved by using this approach. The RS temperature bias is calculated as the difference between the RO and RS departures, i.e.

$$\overline{O_{RO} - O_{RS}} \approx \overline{O_{RO} - B_{RO}} - \overline{O_{RS} - B_{RS}} \quad (2.1)$$

where  $O$  is the observation and  $B$  is the background, forward-modeled into observation space. The  $\approx$  denotes that the assumption has been made that  $B_{RO}$  and  $B_{RS}$  are equally representative of the true values at the RO and RS locations respectively, i.e the central assumption is that the NWP forecast bias does not vary between the RO and RS locations. This is a more

robust assumption compared to direct co-locations between measurements, which are made assuming that the atmosphere does not vary over the separation distance. A similar double differencing approach is used by Haimberger et al. [8] to homogenize radiosonde temperature records.

In the following sections the linear Abel transform, the hydrostatic integration and the calculation of the Tdry from pressure and refractivity is described. As provided by Sean Healy (personal communication), a tangent linear version of the equations is used to calculate the RO O-B statistics in Tdry space. Healy's version is based on the linear calculations developed in Syndergaard [34], who originally proposed this in order to assess error propagation in the retrieval chain.

## 2.1 Linear Abel transform

With the assumption of local spherical symmetry of the atmospheric refractive index (Kursinski et al. [17]), the spherical equivalent of Snell's law is known as Bouguer's law:

$$nr \sin \Phi = \text{const.} = a \quad (2.2)$$

where  $n$  is the refractive index,  $r$  is the radial distance from the centre of curvature and  $\Phi$  is the angle between the ray vector and the local radius vector. At the tangent point, where the ray is parallel to the surface,  $\Phi = \frac{\pi}{2}$ , and therefore the refractive index times the tangent radius equals the impact parameter,  $a$ , which is a constant for a given ray and represents the distance of closest approach of the undeflected ray from the local centre of curvature.

$$nr = a \quad (2.3)$$

The relation between the BA,  $\alpha$ , and the refractive index  $n$  as a function of radial distance is described by the Abel transform (see Fjeldbo et al. [6]), which is valid under the assumption of local spherical symmetry.

$$n(r) = \exp \left( \frac{1}{\pi} \int_x^\infty \frac{\alpha(a)}{\sqrt{a^2 - x^2}} da \right) \quad (2.4)$$

where  $r$  is the tangent radius (radial difference from centre of curvature to the tangent point)  $a$  is the impact parameter and  $x = nr$  equals the impact parameter for the radius  $r$ , based on the local spherical symmetry assumption (eq. 2.3).

Due to the inconvenience that the refractive index  $n$  for L-band frequencies is close to 1 and to better relate it to the density, the refractivity is defined as:

$$N = 10^6(n - 1) \quad (2.5)$$

Based on equation 2.4, Syndergaard [34] developed a linear version of the Abel transform, assuming linear variation of the BA between successive observation levels. The linearisation of equation 2.4, (disregarding the factor  $10^6$ ) gives the refractivity as a function of the impact

parameter  $a$ .

$$N(r) = \frac{1}{\pi} \int_x^{\infty} \frac{\alpha(a)}{\sqrt{a^2 - x^2}} da \quad (2.6)$$

Discretising equation 2.6 (see Appendix in Syndergaard [34]) gives:

$$\mathbf{N} = \mathbf{A}\boldsymbol{\alpha} \quad (2.7)$$

with  $\mathbf{A}$  being the  $m \times m$  triangular matrix, where  $m$  is the dimension of the profile:

$$A_{ij} = \begin{cases} 0 & \text{if } j < i \\ -\frac{1}{\pi(a_{i+1}-a_i)} \left[ \sqrt{a_{i+1}^2 - a_i^2} - a_{i+1} \ln \left( \frac{a_{i+1} + \sqrt{a_{i+1}^2 - a_i^2}}{a_i} \right) \right] & \text{if } j = i \\ \frac{1}{\pi} \left\{ \frac{1}{a_j - a_{j-1}} \left[ \sqrt{a_j^2 - a_i^2} - \sqrt{a_{j-1}^2 - a_i^2} - a_{j-1} \ln \left( \frac{a_j + \sqrt{a_j^2 - a_i^2}}{a_{j-1} + \sqrt{a_{j-1}^2 - a_i^2}} \right) \right] \right. \\ \left. - \frac{1}{a_{j+1} - a_j} \left[ \sqrt{a_j^2 - a_i^2} - \sqrt{a_{j+1}^2 - a_i^2} - a_{j+1} \ln \left( \frac{a_{j+1} + \sqrt{a_{j+1}^2 - a_i^2}}{a_j + \sqrt{a_j^2 - a_i^2}} \right) \right] \right\} & \text{if } j > i \end{cases}$$

This linear version of the Abel transform is used in this study to calculate the refractivity from the observation and background BAs. For each profile, the BA value at the highest level is used to initialise a (fairly arbitrary) extrapolation to allow the computation of the Abel integral up to infinity in order to obtain the refractivity at this height and below. Then the refractivity at the highest level is used to initialise the hydrostatic integral to obtain Tdry at all levels below. In other words, each value of Tdry contains information from every value of refractivity above, and each of these refractivity values contains information from the BA at the highest level and above. Hence there is considerable sensitivity of the Tdry values to the highest values of BA which are dominated by a priori information.

### 2.1.1 The tangent linear Abel transform

The matrix  $\mathbf{A}$  can also be used to propagate BA departures (RO O-Bs), since

$$\mathbf{N}_2 - \mathbf{N}_1 \simeq \mathbf{A}\boldsymbol{\alpha}_2 - \mathbf{A}\boldsymbol{\alpha}_1 = \mathbf{A}(\boldsymbol{\alpha}_2 - \boldsymbol{\alpha}_1) \quad (2.8)$$

is valid for two BAs that are sufficiently similar and where  $\mathbf{A}$  is similar for both linearisation states. This tangent linear version of the Abel transform can be expressed in the same notation as equation 2.7:

$$\delta\mathbf{N} = \mathbf{A}\delta\boldsymbol{\alpha} \quad (2.9)$$

In our case the observed and model BAs are co-located and therefore sufficiently similar to consider the matrix  $\mathbf{A}$  to be equal for the observation and model BA. Therefore this tangent linear version of the Abel transform, where the BA departures are used to calculate the refractivity departures, is acceptable.

The linear approximation of non-linear functions gives a good estimate of the value, as long as the departure from the linearisation state is small. TL models are used extensively in data assimilation systems (Hoffman et al. [14]), e.g. to estimate the development of the atmo-

spheric state at short time scales, as well as in observation operators. To build the tangent linear version of code, the partial derivative of each equation is calculated one after another avoiding the need to compute the **A** matrix in its entirety.

The tangent linear Abel transform together with the tangent linear version of the Tdry calculation is used throughout this report.

## 2.2 Tdry calculation

The relation between refractivity  $N$ , temperature  $T$ , pressure  $P$  and water vapour pressure  $P_w$  is described in the Smith-Weintraub equation ([30])

$$N = c_1 \frac{P}{T} + c_2 \frac{P_w}{T^2} \quad (2.10)$$

where  $c_1 = 77.6 \frac{K}{hPa}$  and  $c_2 = 3.73 \times 10^5 \frac{K^2}{hPa}$  are empirical constants.

In a dry atmosphere, the second term is zero. The next subsection describes how a refractivity profile is used to calculate the pressure with hydrostatic equation and ideal gas law (assuming no water vapour) and how the Tdry is calculated with first term of the the Smith-Weintraub equation.

### 2.2.1 Hydrostatic integration

In this study we use a method for the ‘linear Tdry calculation’, where the hydrostatic equation is integrated, assuming a gravitational acceleration that varies with latitude and altitude.

Here the method is explained in detail, starting with the hydrostatic equation:

$$dP = -\rho g dz \quad (2.11)$$

where  $P$  is the pressure,  $\rho$  the density of air,  $g$  the gravitational acceleration and  $z$  the geopotential height. Furthermore the ideal gas law describes the dependence of the pressure on the specific gas constant  $R$ , the temperature  $T$  and the density  $\rho$ :

$$P = \rho RT \Leftrightarrow \rho = \frac{P}{RT} \quad (2.12)$$

Taking into account only the dry, neutral part of the atmosphere, where the Tdry is equivalent to the physical temperature ( $T = T_{dry}$ ), the Smith-Weintraub equation (2.10) becomes:

$$N = c_1 \frac{P}{T_{dry}} \quad (2.13)$$

the density can be expressed as:

$$\rho = \frac{N}{Rc_1} \quad (2.14)$$

which leads to the following formulation of the hydrostatic equation:

$$dP = -\frac{N(z)}{Rc_1} g dz \quad (2.15)$$

Assuming  $N$  varies exponentially with geopotential height within the  $i^{th}$  layer of the refractivity profile as follows:

$$N(z) = N_i e^{-k_i(z-z_i)} \quad (2.16)$$

The refractivity value at the level above allows the inverse scale height  $k_i$  to be calculated:

$$\begin{aligned} N_{i+1} &= N_i e^{-k_i(z_{i+1}-z_i)} \\ \rightarrow \ln\left(\frac{N_i}{N_{i+1}}\right) &= k_i(z_{i+1} - z_i) \\ \rightarrow k_i &= \frac{\ln\left(\frac{N_i}{N_{i+1}}\right)}{z_{i+1} - z_i} \end{aligned} \quad (2.17)$$

The hydrostatic equation to be integrated for the  $i^{th}$  layer, reads:

$$\int dP = -\frac{g}{Rc_1} N_i \int e^{-k_i(z-z_i)} dz \quad (2.18)$$

Integration of the hydrostatic equation from  $z_{i+1}$  to  $z_i$  gives

$$\begin{aligned} \int_{z_{i+1}}^{z_i} dP &= \frac{g}{Rc_1} N_i \left[ \frac{1}{k_i} e^{-k_i(z-z_i)} \right]_{z_{i+1}}^{z_i} \\ &= \frac{g}{Rc_1 k_i} N_i \left[ e^{-k_i(z_i-z_i)} - e^{-k_i(z_{i+1}-z_i)} \right] \\ &= \frac{g}{Rc_1 k_i} [N_i - N_{i+1}] \end{aligned} \quad (2.19)$$

and with  $k_i$  as in equation 2.17 this gives:

$$\Delta P = \frac{g}{Rc_1} \frac{N_i - N_{i+1}}{\ln\left(\frac{N_i}{N_{i+1}}\right)} (z_{i+1} - z_i) \quad (2.20)$$

The calculation of the pressure at each impact height level, is initiated at the highest level, which requires a priori knowledge about the temperature at this level. The a priori temperature assumed in this study is a mean value of the model temperature at the geopotential height level 59.060 km which is closest to the highest impact height level. The average includes all those model values at 59.060 km that are co-located with the RO BA profiles which are used to calculate the mean RO O-B for a given RS site. Given this temperature, the top level pressure is calculated as  $P = \frac{NT}{c_1}$ .

Given the pressure (calculated as above) and the Abel-derived refractivity at a particular level,  $T_{dry}$  can be calculated with the dry part of the Smith-Weintraub equation:

$$T_{dry} = c_1 \frac{P}{N} \quad (2.21)$$

As for the linear Abel transform, a tangent linear version of the entire  $T_{dry}$  calculation, comprising the hydrostatic integration and the Smith-Weintraub equation is used in this study. The calculation of the  $T_{dry}$  departure can be expressed with the linear  $T_{dry}$  operator  $\mathbf{K}$  and

the BA departure as:

$$\delta T = \frac{\partial T}{\partial \alpha} \delta \alpha = \mathbf{K} \delta \alpha \quad (2.22)$$

where the  $\mathbf{K}$  matrix is the matrix of partial derivatives of the Tdry with respect to bending angle, assuming all other a priori information required in the retrieval is fixed.

A calculation with the original non-linear equations is done only for the purpose of comparison and to linearise successive parts of the retrieval chain. The two different versions of calculating the Tdry increment (RO O-B Tdry) from the BA increment (RO O-B BA) are summarised below.

### 1. Calculation with tangent linear equations

The refractivity increment (O-B refractivity) is calculated with the tangent linear version of the Abel transform (eq. 2.8), which requires the BA increment (RO O-B) as input and in addition the mean RO BAs as linearisation state. The tangent linear version of the hydrostatic integration and the Smith-Weintraub equation are used to calculate the Tdry increment from the refractivity increment.

### 2. Calculation with non-linear equations

The refractivity is calculated separately for the observation and model BA with the linear Abel transform (eq. 2.4). The full non-linear hydrostatic integration and the Smith-Weintraub equation (eq. 2.10) are applied to the model and the observation refractivity separately. In a final step the Tdry retrieved from the background BAs is subtracted from the Tdry retrieved from the observed BA giving an estimate of the RO O-B Tdry.

## 2.3 Performance of the dry temperature calculation

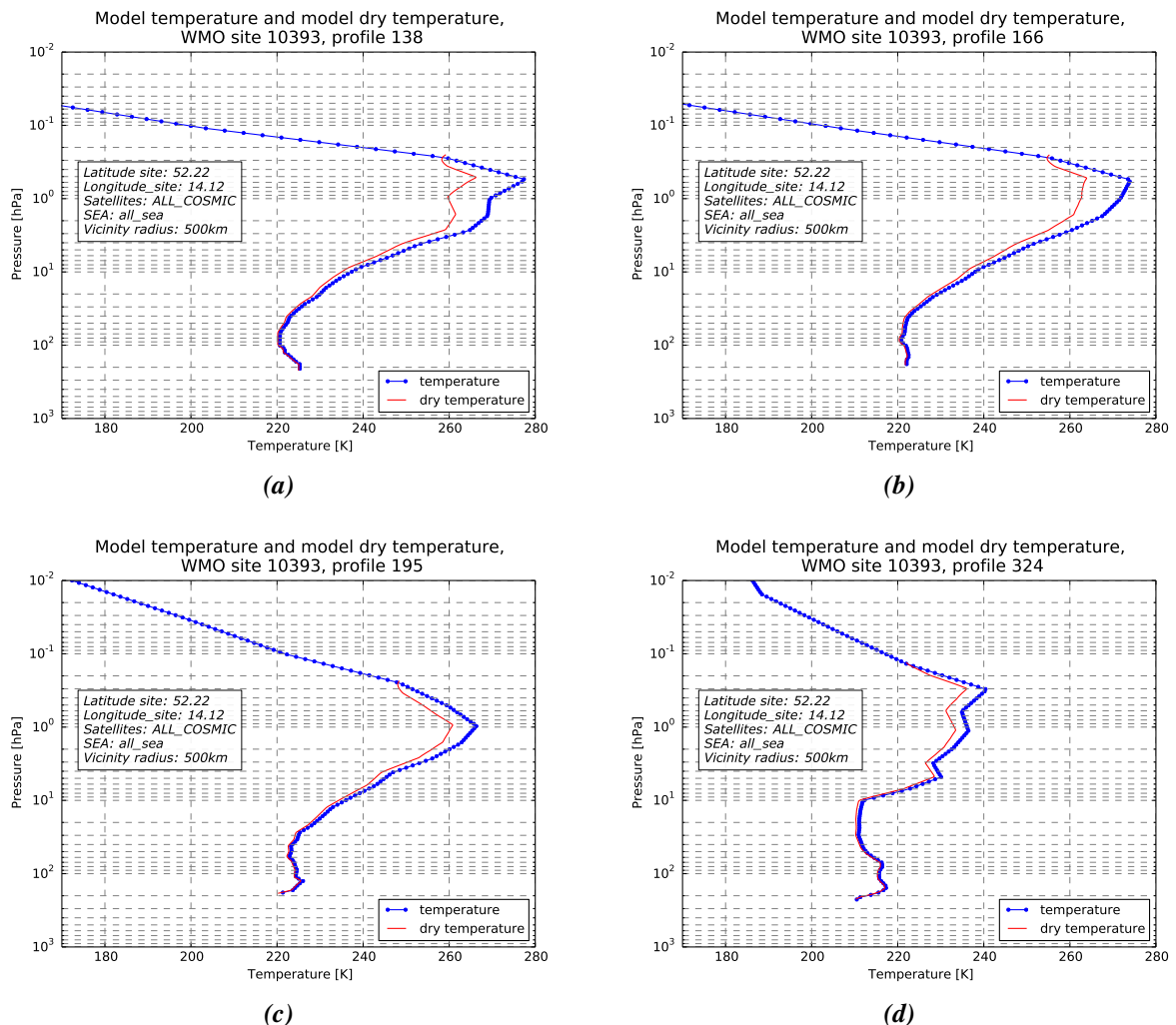
The Tdry calculation used here, which is based on the linear Abel transform and the integration of the hydrostatic equation, is tested in this section. Since the model BAs are calculated from the model variables as described in Burrows et al. [3], it is possible to test the performance of the Tdry calculation by comparing one model temperature profile with the Tdry profile retrieved from the associated model BA. Tdry is computed with the non-linear version of the equations. If the assumptions in the forward (temperature to BA) and inverse (BA to temperature) calculations were identical, the differences of model temperature and model Tdry would be negligible in the dry atmosphere, but because of differing assumptions, differences that vary with altitude are expected. This is due to extrapolation above the highest observed bending angle, and differing assumptions about the variation of the quantities between levels (compare Burrows et al. [3] and section 2.1).

Figure 2.1 shows the background temperature (blue)<sup>1</sup> and the Tdry (red) retrieved from the associated background BA for four profiles chosen arbitrarily around the German example site (see table 4.1). The profiles comprise pressure levels with negligible humidity, as determined following section 4.1. In each case (a) to (d), the background and retrieved temperature profiles at the lower levels are very similar, but the differences increase higher

<sup>1</sup>Note that in the Met Office forward model the temperature is derived from the model pressure and specific humidity, assuming hydrostatic balance. This derived temperature is used here as ‘background temperature’; the difference between this and the true model temperature is small, see Rennie [25].

in the atmosphere. Different assumptions in the forward and inverse calculation, particularly about the portion of refractivity above the highest observation, cause the differences around 1 hPa, with a decreasing influence towards the lower levels. At the highest observation level Tdry agrees well with the background temperature, emphasising the result of initialising the hydrostatic integration at the highest level with the model temperature as described in 2.2.1. At (a), (b) and (c) the highest temperature is plotted at slightly too high dry pressure values compared to the model pressure, which again is caused by different assumptions in the calculation of the pressure in model and Tdry calculation.

The non-linear Tdry calculation as described in chapter 2 performs well, however, differences in the model temperature and Tdry are present due to differences in the assumptions. From now on the tangent linear version of the Tdry calculation will be used for most computations. Chapter 4.2 discusses inter alia how the tangent linear code is performing compared to the non-linear Tdry computation.



**Figure 2.1:** Background temperature and Tdry comparison for individual profiles from around the German example site (see table 4.1). Tdry is calculated from the background BA using the non-linear calculation, see numeration in 2.

## 3 Data and Model

### 3.1 Radio occultation data

The signal transmitted by the GNSS at about 20,000 km altitude is received by a Low Earth Orbit (LEO) satellite. The measurement are made during the radio occultation event, e.g. when the GNSS satellite rises or sets behind the horizon. In this case the signal is going through the limb of the atmosphere, where it is bent and delayed before it is received by the LEO satellite. The measured phase shift of the received signal, allows the retrieval of atmospheric variables, mainly Tdry, dry pressure and, given further a priori knowledge about the atmospheric state, the water vapour. Since the temperature and pressure values are retrieved assuming that water vapour is negligible, these quantities are often referred to as Tdry and dry pressure, respectively, by the RO community. A description of the RO technique can be found in Kursinski et al. [18, 17]. Since the basic measurement is based on precise timing available from atomic clocks, it offers the possibility to be traceable to the international SI standard of time (Leroy et al. [20]). This ensures the long-term stability and reproducibility of RO data and makes them valuable for climate studies.

Thousands of RO profiles are measured every day and provide a global coverage. While the vertical resolution of 100 m - 1 km is comparably high, the horizontal scale is big, comprising 100-300 km around the tangent point (see figure 3 in Anthes [1]). BA profiles can be retrieved from the measured phase shift of the GNSS signal, which implies that they are comparably raw measurement assuming local spherical symmetry. In contrast to other remote sensing techniques RO measurements are nearly independent of the weather conditions and the profiles are retrieved from the higher atmosphere down into the boundary layer, the lowest layer of the atmosphere. An overview of the characteristics of RO measurements can be found in Anthes [1].

This report concentrates on the near real time data of the US-Taiwanese Constellation Observing System for Meteorology, Ionosphere, and Climate (COSMIC) - FORMOSAT-3 mission (here referred to simply as COSMIC), but the sensitivity study investigates the possibility to use additional data from the two GNSS Receiver for Atmospheric Sounding (GRAS) instruments onboard the Metop satellites.

To analyse RO and RS departures on a common pressure grid, the RO Tdry profile is interpolated to the 16 standard pressure levels (on which TEMP data are provided) as shown in section 3.2 and one additional pressure level above and below is added for the RO data set.

#### 3.1.1 Quality control RO

In a preprocessing step prior to assimilation, the bending angle profiles are assessed for their quality. Central to this procedure is a 1D-Var algorithm that uses co-located model background information to obtain an optimal solution for each observation profile. Complete profiles are flagged for rejection if (i) the 1D-Var fails to converge in 20 iterations, (ii) the initial cost function (2J/m) is greater than 2.5 or (iii) the final cost function, i.e. at convergence, is greater than 2.0. Also, bending angle observations are rejected on a level-by-level basis if the absolute value of the observation minus the 1D-Var solution is greater than the assumed observation error multiplied by 5.

The values in the (conservative) rejection criteria and the number of iterations required were

chosen based on experience. Approximately 10% of the RO profiles are rejected. Furthermore, BAs are rejected on a level-by-level basis if the absolute value of the observation minus the 1D-Var solution is greater than the assumed observation error multiplied by 5.

### 3.1.2 The RO temperature null-space

It should be emphasized that RO is not a direct measurement of temperature, and some *a priori* information is required to make a temperature retrieval well-posed. The need for *a priori* information implies that there is a RO measurement "null-space", meaning there are some atmospheric profile perturbations that do not affect the measured values. Conversely, information about these perturbations cannot be retrieved directly from the measurement alone (see Rodgers [27], section 2.2.1).

In the context of RO, in the stratosphere, where moisture can be neglected, BA and refractivity values are related to density as a function of height. As a consequence, temperature perturbations for which the amplitude grows exponentially with the density scale height are difficult to detect with RO, because they do not affect the density as a function of height significantly. Temperature perturbations which grow exponentially in this way quickly produce unphysical temperature values on height levels. However, more subtle perturbation patterns – partly composed of this exponential growth – remain potentially problematic. For example, the temperature bias highlighted by Steiner et al. [31, see Figure 8b], produced by perturbing the *a priori* information used in their geophysical retrieval, is in the RO measurement null-space.

It is important to be aware of this fundamental limitation of the RO measurements. The technique presented here will only be able to estimate the contribution to the RS biases that the BA observations can determine uniquely. The assimilation of RO in NWP systems (Healy [11]) and reanalysis (Poli et al. [24], Simmons et al. [29], Kobayashi et al. [16]) is seen to anchor the temperatures at around 100 hPa, which is an indication that RO is able to provide useful bias information at these levels.

## 3.2 Radiosonde data

More than 800 upper-air sites launch RS on weather balloons to measure vertical profiles of temperature, humidity and, depending on the RS type, pressure. Many manufacturers correct the radiation bias in the RS temperature and humidity profiles before the data are released. Even after this correction, the temperature profiles can have substantial biases that vary with the solar elevation angle (SEA), but also depend on post-flight processing applied at the ground station. The RS temperature bias is commonly calculated per sonde type [see e.g. 10, 33, 32], though [22] found a variation of the temperature bias for stations launching the same sonde type, supporting our approach to calculate the bias separately for each station. An thorough evaluation of sources of biases in RS measurements can be found in [5]. Here we provide a method to correct the remaining temperature bias prior to assimilation into NWP models. Here we aim to calculate bias corrections for RS temperature profiles which may be applied prior to assimilation into NWP models. Therefore most RS launch sites which regularly provided data to the Global Telecommunication System (GTS) and passed the operational quality control of the Met Office Observation Processing System (OPS) in 2014 are analysed here. To count as a regular upper-air site, i.e. for inclusion in this study,

a minimum of 15 RS profiles launched at the same position must be available from at least one month of 2014, which means that mobile ship launches or stations launching only a low number of sondes are ignored. In contrast to most countries, Russian upper-air sites mainly launch RS without a pressure sensor and calculate the pressure with the hydrostatic equation from temperature, humidity and height, which is measured with a radar. At least three different radar systems with varying processing software are used; the older AVK and the newer MARL and Vector radar. Most Russian RS types have two versions that differ only in their carrier frequency to be compatible with the different radar systems (Bruce Ingleby, personal communication). Due to the limited capacity of the WMO RS type list in World Meteorological Organization [36], the MARL-A and Vector-M radar share one code and can not be separated. Code 90 that is specified as “unknown, not specified” actually includes three more Russian RS types, namely I-2012, MRZ-3MK, AK2m (Bruce Ingleby, personal communication). RS temperature profiles in TEMP format used nowadays are submitted on significant pressure levels and the fixed set of standard pressure levels. In this investigation the temperature bias is calculated at those standard pressure levels of RS profiles submitted in the alphanumeric TEMP format (i.e. 1000 hPa, 925 hPa, 850 hPa, 700 hPa, 500 hPa, 400 hPa, 300 hPa, 250 hPa, 200 hPa, 150 hPa, 100 hPa, 70 hPa, 50 hPa, 30 hPa, 20 hPa and 10 hPa) that have negligible humidity. In the Met Office NWP system TEMP profiles have a cold bias of -0.05 K that is caused by the conversion from degree Celsius to Kelvin (see Ingleby and Edwards [15]). Additionally the encoding/decoding of the RS measurement in TEMP format causes an offset, e.g. -0.095 K for the RS92 with DigiCORAIII processing (see Ingleby and Edwards [15]) which leads to a combined bias of almost -0.15 K in the RS92 data within the Met Office NWP system.

### 3.2.1 Quality control RS

Outliers in the RS dataset are rejected based on the Median Absolute Deviation (MAD) criterion. While the mean value and the standard deviation (SD) are especially sensitive to outliers and are therefore problematic for detection of outliers, the MAD presents a robust measure to detect outliers. The MAD is calculated for each standard level separately giving different outlier criteria for each level. First the temperature difference between the RS observation and the model background (RS O-B) is calculated for all profiles at one upper-air site. Then the absolute deviation is calculated by subtracting the median of all RS O-B from each RS O-B profile. The median value of the absolute deviation at one standard pressure level is the MAD for the given standard pressure level. Based on [21] a moderately conservative threshold of 2.5 is chosen to reject outliers, which means that the RS temperature at a certain level is rejected if the RS O-B is more than  $2.5 \times \text{MAD}$  away from the median of all RS O-B's at that level.

### 3.3 Model

The Met Office global NWP system serves as a transfer medium by providing the model background for the RO and RS profiles. Using a model as transfer medium reduces differences that are entirely caused by imperfect co-locations.

During the investigated year, 2014, the model was due for an update of the dynamical core

from the version described in Davies et al. [4] to a version described in Walters et al. [35]. As a result, the resolution changed on the 15 July from N512L70 to N768L70. This corresponds to a decrease in the grid length from about 25 km in mid-latitudes to about 17 km. Also, the time step decreased from 10 minutes to 7.5 minutes.

## 4 Sensitivity study

As stated in the introduction, pragmatic decisions are needed in this project, to eliminate some degrees of freedom in the estimation of RS biases. This chapter illustrates the sensitivity of the diagnostic statistics to certain parameters and explains the decisions that led to the final set-up for the estimation of RS biases based on RO data. Here, five example sites, summarised in table 4.1, are analysed, comprising different climate regimes.

Country	Latitude	Longitude	Station ID	RS/radar type
Germany	52.22	14.12	10393	Vaisala RS92
Russia (West)	69.35	88.27	23078	AVK-AK2-02, MARL-A/Vektor-M AK2-02, MARL-A/Vector-M-BAR
Russia (East)	59.55	150.78	25913	MARL-A/Vektor-M AK2-02, AVK-BAR, MARL-A/Vector-M-BAR, "unknown"
Indonesia	-1.18	136.12	97560	Meisei
Antarctica	-69.0	39.58	89532	Meisei

**Table 4.1:** Longitude, Latitude, World Meteorological Organization (WMO) station identifier (ID) and RS/radar type for the example upper-air sites analysed in this report. The RS type "unknown" actually includes three more Russian RS types, namely I-2012, MRZ-3MK, AK2m (Bruce Ingleby, personal communication).

The wide scope of this study presents a large number of options as to which parameters are used. Here, we discuss the choices that have been made and analyse the sensitivity to some of the following parameters to justify the setup of the study:

1. Lowest level at which bias corrections are calculated
2. Upper cut-off criterion for RO departures (here cut-off means setting them to zero)
3. Vicinity radius centred on the radiosonde sites
4. Setting or rising occultations
5. Solar elevation angle (SEA) of RO and RS
6. Different RO missions

The influence of the different parameters is described in the following sections.

### 4.1 Determining the lowest dry level

Since output from a NWP model is used as a transfer medium, it is possible to determine the lowest level of negligible humidity in the background fields separately for each RO profile, enabling us to use the Tdry profile as low in the atmosphere as is reasonable. The metric used to determine the deviation of the Tdry from the actual temperature is described in [28] as:

$$T_{dry} - T \approx -4/5c_{q2T}q \quad (4.1)$$

where  $q$  is the model specific humidity and  $c_{q2T} = \frac{c_2/c_1}{a_w} = 7728 \frac{kg}{kg}$ .  $a_w$  is the ratio of the dry air to water vapour gas constants,  $c_1$  and  $c_2$  are the constants used in the Smith-Weintraub

equation (see eq. 2.10). This basic estimate is obtained from equation (16) in Scherllin-Pirscher et al. [28]:

$$T_{dry} - T \approx T \left( \frac{P_{dry} - P}{P} - \frac{c_{q2T}q}{T} \right) = -c_{q2T}q \left( 1 - \frac{(P_{dry} - P)}{P} - \frac{c_{q2T}q}{T} \right) \quad (4.2)$$

The fraction in the rightmost parenthesis of equation 4.2 is approximately constant with a value of  $\approx 0.2$ , which leads to the simple estimate of the dry temperature increment in equation 4.1.

The lowest level at which, and above where, the difference in  $T_{dry} - T$  stays below 0.09 K is detected for each single profile. This value is chosen based on the suggestions in Scherllin-Pirscher et al. [28] and also figure 2.1 supports this decision, since the original model temperature and the temperature retrieved with the tangent linear version for all dry levels agree well in the lower levels. Depending on the latitude and the atmospheric conditions the lowest dry level will be reached at a different pressure level. If an appropriate amount of ‘dry’ profiles exists at a certain level the RO O-B statistics and the mean RO BA are calculated. In order to use the RO data as low in the atmosphere as possible, the minimum amount of data for the lowest levels is set to a comparably low value of 10. Since the RS temperature bias corrections (chapter 5) are presented with the associated standard errors, which depend on the sample size, it is possible to make a decision as to whether the bias correction is meaningful. Though at the lowest levels, the bias corrections are not representative for all atmospheric conditions at the respective site, as the included RO profiles are sampled in especially dry conditions, which could lead to particular bias characteristics in the RO departures, probably originating from the model.

For  $T_{dry}$  departures at a given level there is an important difference between the BA departures above and below this height. The former values influence the  $T_{dry}$  departures, but the latter do not (see section 2.1). The RO departures in the highest levels have a particularly large influence and will be set to zero as described in section 4.2.

## 4.2 Upper cut-off criterion for RO bending angles

Since this study focuses on a pressure range from about 400 hPa to 10 hPa, and based on the possibilities the tangent linear calculations offer, different upper impact heights above which all BA departures are set to zero, are tested. Because the  $T_{dry}$  retrieval algorithm is a vertical integral, a carefully chosen upper threshold will limit the downward propagation of model information which would otherwise result in an inconsistency between the background values used for the departure statistics of the two observation types. Further implications will be studied in section 4.2.2.

The upper impact height cut-off is analysed from 20 km to 55 km in 5 kilometre steps and also the effect of removing the very highest value is investigated. Above the cut-off, the BA departure values are set to zero, which means that the resulting  $T_{dry}$  departures will only have a dependence on the BA departures below this height. The results in figure 4.1 show a strong dependence on the upper cut-off impact height for all stations. Furthermore, all locations are most strongly affected by setting solely the highest RO BA departure value to zero before being used in the tangent linear  $T_{dry}$  calculation. For most of the stations (e.g. both

Russian sites) the Tdry departures are converging with decreasing upper cut-off leading to similar results for a cut-off between 20 km and 40 km, but this is not visible at the Indonesian site, The departures calculated with a cut-off at 20-30 km do not reach the highest pressure level where the RS bias will be estimated (10 hPa) and can therefore not be used for this investigation. Based on the results we decide to use a cut-off height of 35 km to minimise the effect of biased model data above 10 hPa. This decision is a compromise and although it might not be optimal, it is very likely to be better than using the non-linear operator.

Section 4.2.2 will in addition analyse the covariance matrices for different cut-off heights and support the decision to use a cut-off height of 35 km.

In addition figure 4.1 shows the RO Tdry departures calculated with the non-linear Tdry operator (orange dashed line), providing an indication of the quality of the linearisation for typical departures. The tangent linear departures without any cut-off are very close to the non-linear departures, which highlights the validity of the tangent linear assumption. It is a clear benefit of the tangent linear code, that the maximum height up to which the BA departures are used in the calculation of the Tdry may be selected to avoid the undesirable influence of arbitrary a priori information on the statistics.

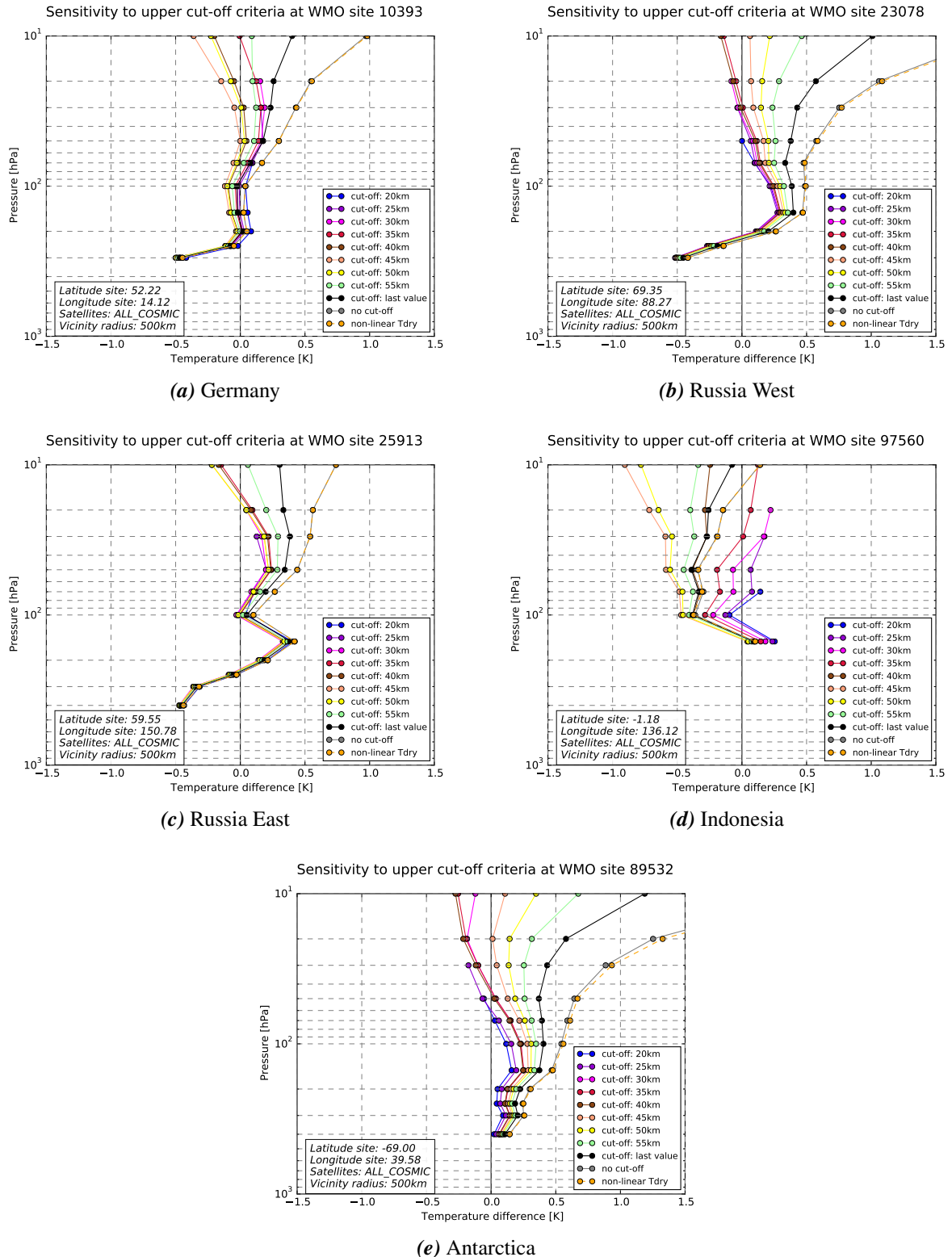


**Figure 4.1:** Sensitivity of the  $T_{dry}$  departures caused by different upper cut-off impact heights (all RO BA departures above the cut-off impact height are set to zero prior to the  $T_{dry}$  calculation).

#### 4.2.1 Influence of the linearisation state

To investigate the influence of the mean observation BA or the mean model BA as linearisation state in the tangent linear calculations, figure 4.2 shows the Tdry departures using the two options. (a) is calculated using the mean observation BA as input and (b) using the mean model BA in the tangent linear Tdry calculation. The figure shows the results for the Indonesian site, but the other example stations show similar results. The differences are very small and from now on the observation BA will be used in the tangent linear Tdry calculation, since biases in RO are expected to be smaller than in the model.

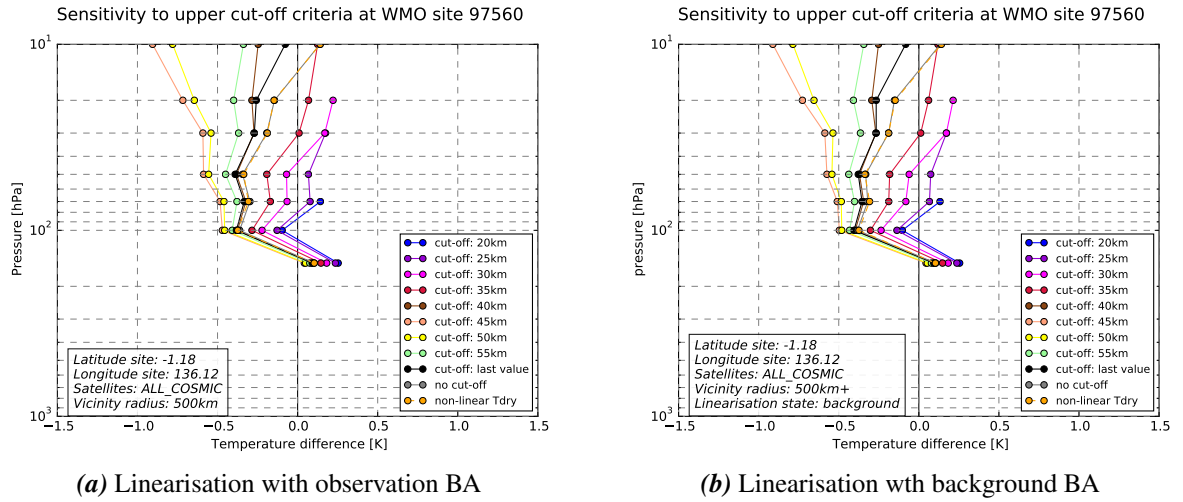


**Figure 4.2:** Difference of using either the RO BA profile (a) or model BA profile (b) as linearisation state for the tangent linear Tdry calculation.

#### 4.2.2 Covariance matrices for different upper cut-off impact heights

To ensure an optimal choice of the upper cut-off impact height, the respective covariance matrices are analysed. An estimate of the population covariance using a finite sample can be calculated with equation 4.3, where  $x$  and  $y$  are variables,  $\bar{x}$  and  $\bar{y}$  are the sample means and  $n$  is the number of sample members.

$$Cov(x,y) = \frac{\sum_{i=1}^n (x - \bar{x})(y - \bar{y})}{n - 1} \quad (4.3)$$

Here we first calculate the covariance for the BA departure profiles using a range of upper cut-off heights, above which the BA departures are set to zero. This is to ensure an optimal choice of the upper cut-off height as described in section 4.2. The BA covariance matrix is then propagated through the Tdry calculation to derive the Tdry covariances.

$$\mathbf{C}_{Tdry} = \mathbf{K}\mathbf{C}_\alpha\mathbf{K}^T \quad (4.4)$$

where  $\mathbf{K}$  is the linear Tdry operator in matrix form,  $\mathbf{C}_\alpha$  is the covariance matrix of BA departures and  $\mathbf{C}_{Tdry}$  is the inferred covariance matrix of Tdry departures.

Figures 4.3 and 4.4 show the covariance matrices calculated from different sub-samples of the BA departures evaluated at the German and Indonesian example sites. The colour scale suits a cut-off at 35 km, which leads to saturation of the colour for the panels with higher impact height cut-offs. The diagonal elements of the covariance matrix are the variances (squared SDs), while the non-diagonal elements indicate the co-variation of the Tdry departures at one level with those at other levels.

Setting only the highest value in the RO O-B BA profile to zero before the propagation of the BA covariances through the Tdry routine, has a big impact on the Tdry covariance matrix (compare figures 4.3(j) and 4.3(i)). The sensitivity to the highest levels is due to arbitrary assumptions on the behaviour of the BAs above the highest level and the retrieved refractivity at the highest level. The retrieval algorithm is a vertical integration, so this a priori information is used multiple times in the computation of Tdry increments at all levels below; hence its dominance at lower levels (though the influence decreases for lower heights), see also section 4.2 . With a further decrease of the upper cut-off impact height, the diagonal elements of the covariance (variance) decrease and the non-diagonal elements, that show a strong positive correlation without any cut-off, decrease until they become slightly negative. Using the tangent linear version of the Tdry calculation enables us to choose the upper cut-off height based on the scope of this project, while the non-linear version would not allow this flexibility. However, choosing the correct upper cut-off impact height is a crucial decision since it influences the results. Since radiosondes only reach pressure levels of about 10 hPa, the aim is to use the minimum amount of data above 10 hPa in order to eliminate the effect of model biases at higher levels. While a cut-off at 30 km is too low to reach the pressure level of 10 hPa for some sites (see fig. 4.1(d)), the impact height of 35 km appears to be a good compromise (see figs. 4.3(d) and 4.4(d)) and is used in this report to calculate the Tdry departures.

Analysing the covariance matrices explicitly shows the benefit of the tangent linear Tdry calculation (see chapter 2). Using the non-linear Tdry calculation would constrain the analysis to the Tdry profiles and the associated covariances calculated without setting high values to zero (see fig. 4.1 grey line, fig. 4.3 (j) and fig. 4.4 (j)). This in fact would lead to a SD of about 7 K at 10 hPa for some upper-air sites, as shown in figure 4.5. Solely setting the highest BA departure to zero decreases the SD to less than half the value. Reducing the cut-off impact height further, leads to continuing decreases in the SD, which is converging to a value of 1-2 K. Using the tangent linear operator with a cut-off at 35 km we are able to achieve a SD that is significant lower compared to the non-linear calculation. Furthermore, the low SD has the effect that the standard error (SE), which indicates the quality of the estimation of the mean, is low. The SE is calculated as  $\frac{SD}{\sqrt{n-1}}$  for both RO and RS and is plotted together with the mean departures in chapter 5.

Also the bias correction, calculated as the difference between RO Tdry departures and RS temperature departures, has a SE, which is calculated following Burns and Dobson [2], as:

$$SE_{Diff} = \sqrt{\frac{\sigma_{RO}^2}{n_{RO} - 1} + \frac{\sigma_{RS}^2}{n_{RS} - 1}} = \sqrt{SE_{RO}^2 + SE_{RS}^2} \quad (4.5)$$

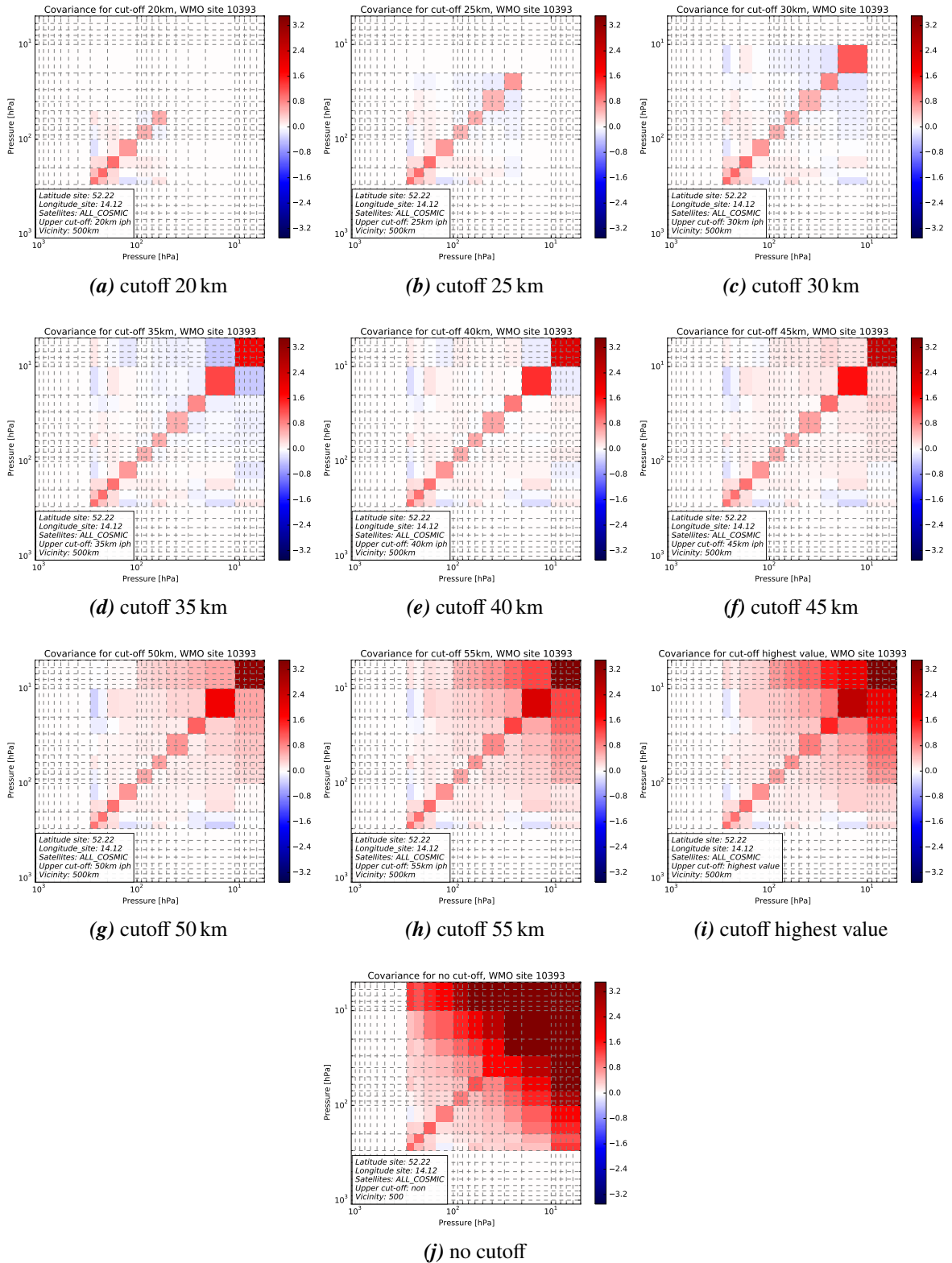


**Figure 4.3:** Tdry departure covariance matrices for different upper cut-off impact heights, German Example site. Colour scale for temperature squared  $[K^2]$  is adjusted to a cut-off at 35 km, which means it is saturated for some higher cut-offs.

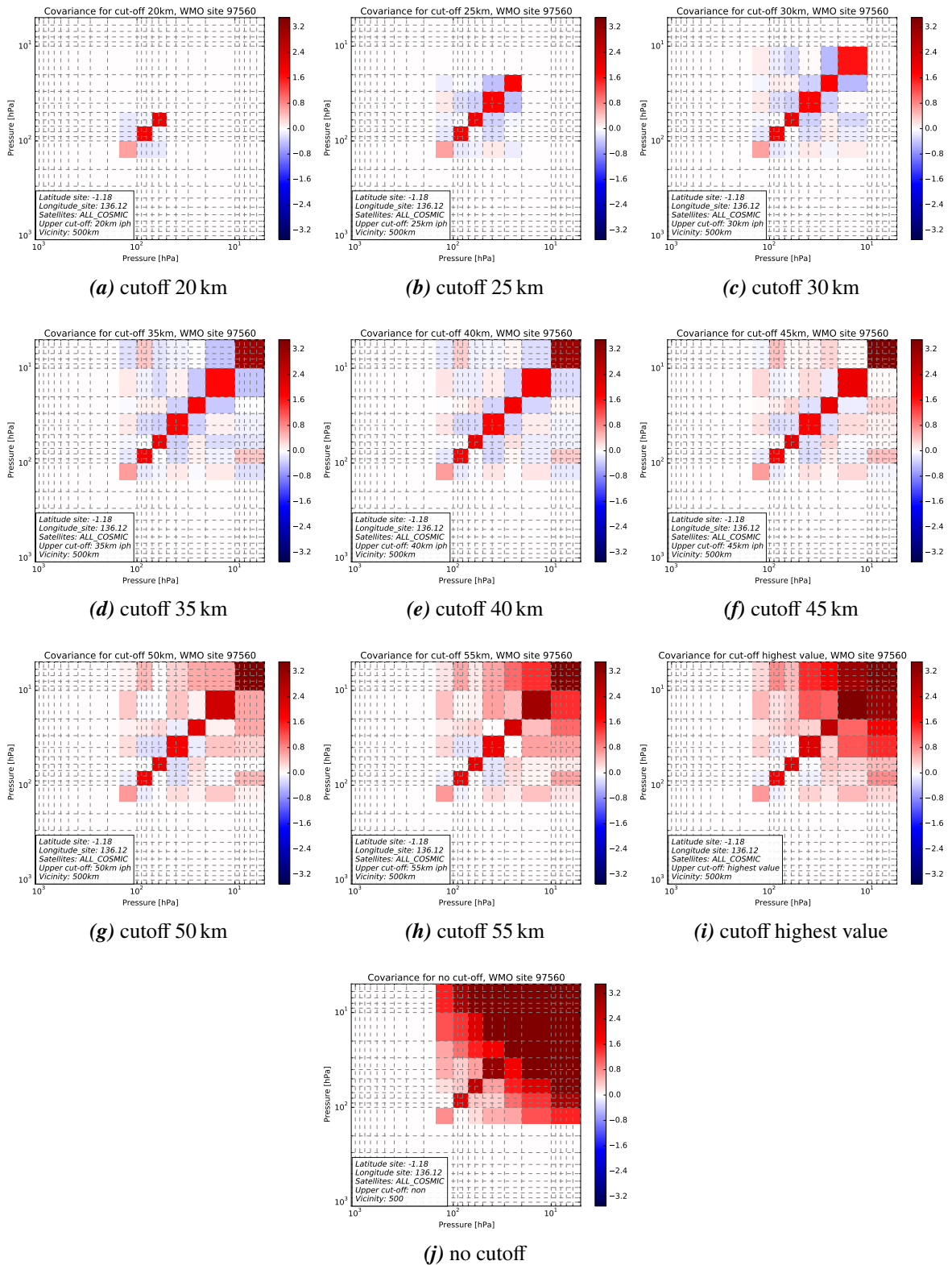


**Figure 4.4:** Tdry departure covariance matrices for different upper cut-off impact heights, Indonesian Example site. Colour scale for temperature squared  $[K^2]$  is adjusted to a cut-off at 35 km, which means it is saturated for some higher cut-offs.

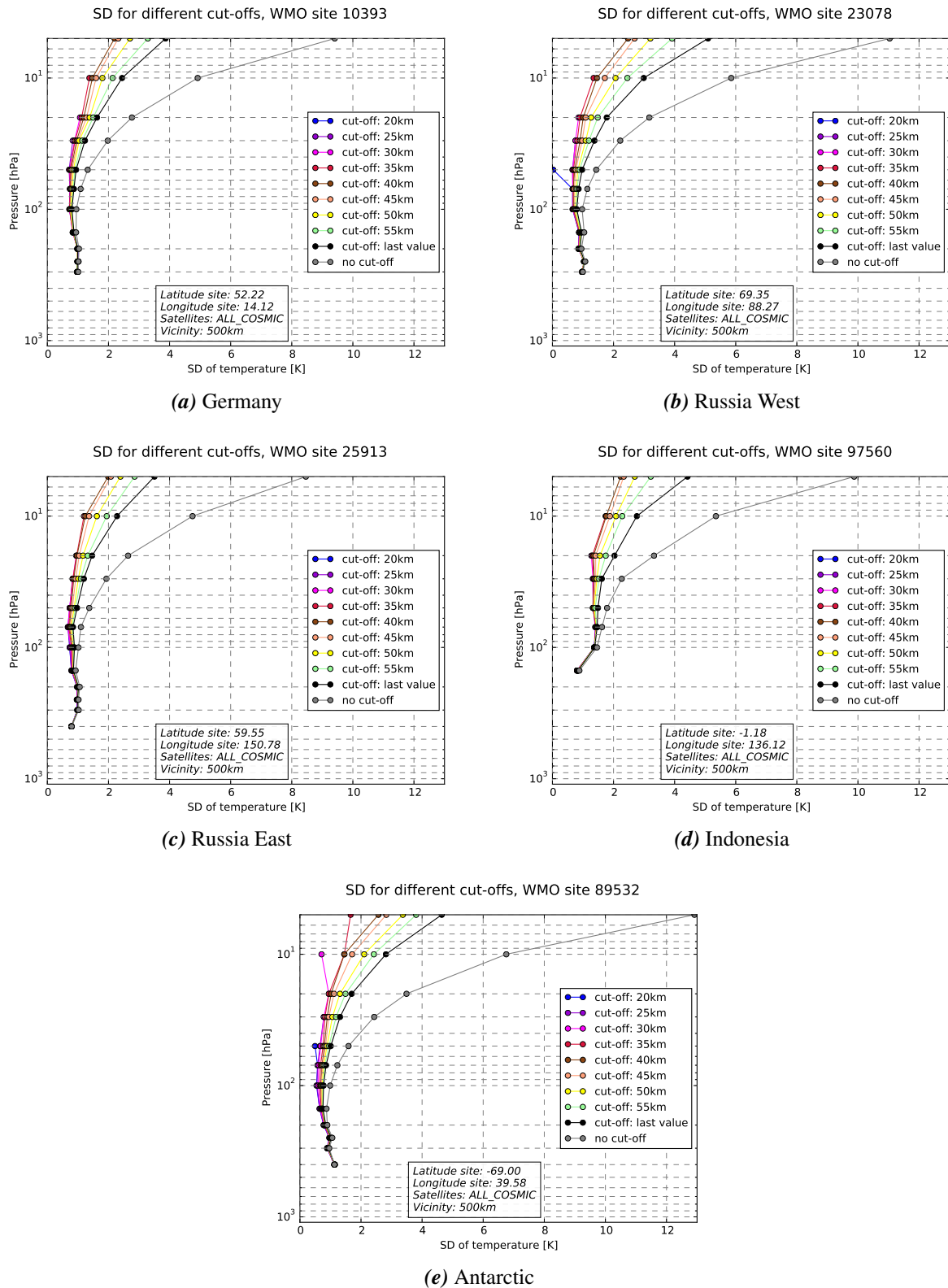
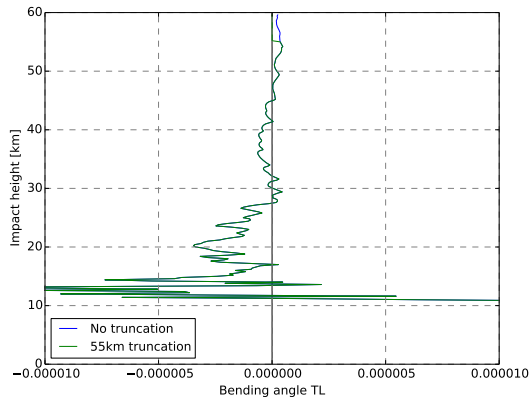


**Figure 4.5:** Standard deviation (SD) of the  $T_{dry}$  departure for different cut-off impact heights.

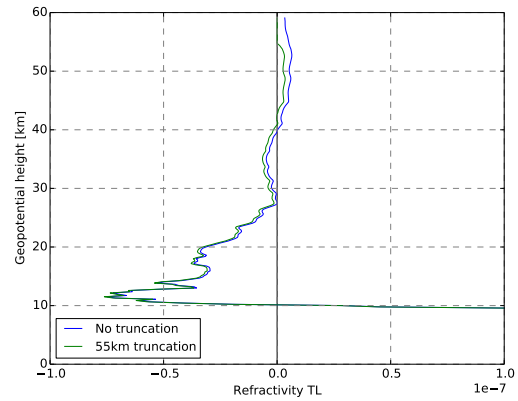
### 4.2.3 Dependence on the highest level bending angle

To understand the strong dependence of the Tdry departures to the cut-off impact height, figure 4.6 shows the different steps in the TL calculation of the Tdry departures, (a) BA departures, (b) tangent linear refractivity departures, (c) tangent linear dry pressure departures, and (d) tangent linear Tdry departures. The variables are plotted for a cut-off height of 55 km (green) and no cut-off (blue).

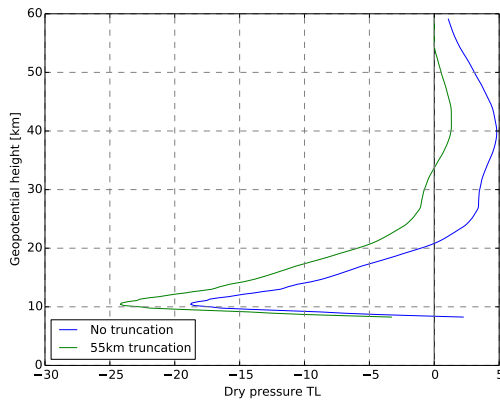
The BA departures (a) show a positive difference of  $(O - B)_{60km}$  compared to  $(O - B)_{55km}$  above 55 km, which leads to a systematic difference in the tangent linear refractivity  $N_{60km} > N_{55km}$  (b) calculated as  $\delta\mathbf{N} = \mathbf{A}\delta\boldsymbol{\alpha}$  (eq. 2.9). The pressure (c) which is calculated as a sum of the top level pressure and the integral of the refractivity as described in section 2.2.1, has a systematic difference for the two cut-offs;  $P_{60km} > P_{55km}$ . Notably the differences in refractivity and pressure are present further down into the atmosphere than the differences in the BA departures. Thus a change in the upper cut-off height results in a different Tdry departure at all levels (d), which is consistent with the influence of systematically different pressure values.



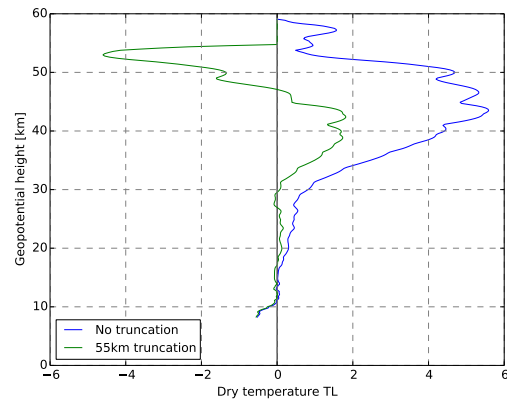
(a) BA background departures in rad



(b) inferred (tangent-linear) refractivity background departures in N-units



(c) inferred (tangent-linear)  $P_{dry}$  background departures in hPa



(d) inferred (tangent linear)  $T_{dry}$  background departures in K

**Figure 4.6:** The different steps in the calculation of the tangent linear  $T_{dry}$  departures for no cut-off (blue) and 55 km cut-off (green).

The propagation of differences in the highest levels further down into the atmosphere can be explained with the Jacobian matrix of  $T_{dry}$  with respect to the BA. The figure 4.7 shows a subset of 3 typical  $T_{dry}$  Jacobians. Each Jacobian shows a sharp spike at the pressure level corresponding to the impact height level of the  $T_{dry}$  retrievals (blue 19 km impact height, pink 29 km impact height, green 39 km impact height), i.e.  $T_{dry}$  at a certain pressure level is highly sensitive to BA at the same pressure level, and those just above. The sharpness of this spike is a feature of the Abel integral transform. However the  $T_{dry}$  is also influenced by the BAs higher up in the atmosphere and especially by the highest BA, as the long tail in the Jacobians (a feature of the hydrostatic integration in the  $T_{dry}$  computation) and the spike at the highest level demonstrates.

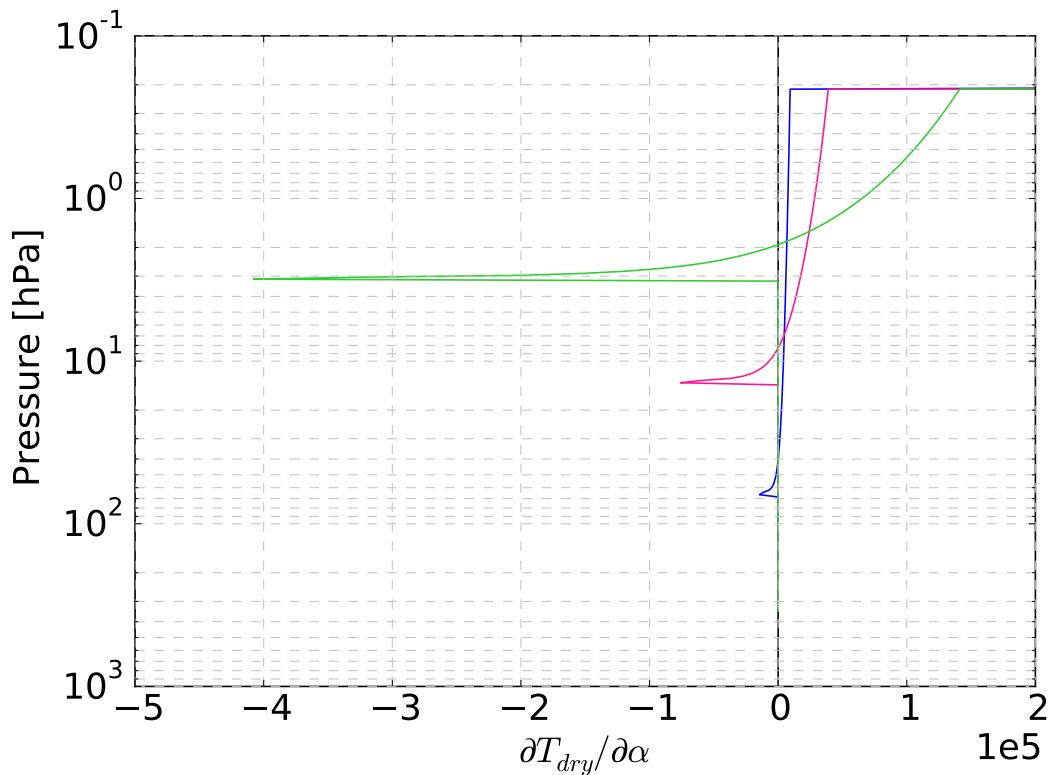


**Figure 4.7:** Subset of a Jacobian matrix (partial derivative) for  $T_{dry}$  with respect to the BAs.

### 4.3 Radius around RS upper-air site

The influence of different radii around the RS launch site for the selection of RO profiles in the vicinity of the RS station, is expected to have a minor influence on the RO O-B statistics. Sun et al. [33] investigated the influence of spatial and temporal mismatch on the mean difference between RS and RO measurements and their SD within a mismatch window of up to 250 km and 6 hours. They found that while the SD increases with an increasing mismatch window, there is no effect on the mean differences on a global scale.

In our study a small influence of increasing vicinity radius can be caused by model biases that depend on the area, and latitude dependent RO biases. One source of area dependent biases in the model is the assimilation of possibly biased measurements that influences the model most strongly in the vicinity of the measurements, with decreasing intensity further away.

Here we analyse vicinity radii of 300 km, 500 km, 1000 km and 2000 km. Figures (not shown here) indicate that the RO profiles are randomly distributed around the five stations. Figure 4.8 shows the influence of the vicinity radii on the mean RO  $T_{dry}$  departures for five different RS launch sites, together with the number of occultations included in the mean RO O-B (dashed lines). The number of measurements increases up to approximately a factor of four if the vicinity radius is doubled.

At most upper-air sites the mean RO  $T_{dry}$  departures are very similar for the different vicinity radii. Only the low-latitude site in Indonesia (d) shows considerable differences in the  $T_{dry}$

departures depending on the vicinity radius around the site. This might be due to the much smaller number of RO profiles which are used to calculate the RO statistics.

To decide which vicinity radius is used in this investigation, the SD for different vicinity radii is plotted in 4.9. While the SD show a chaotic behaviour at some stations (e.g. 4.9(a) and (d)) it has a tendency to slightly increase with increasing radius at other stations (e.g. 4.9(e)). Therefore for the further investigation a vicinity radius of 500 km is used, which is a compromise between having a sufficient sample size while keeping the SD as low as possible.

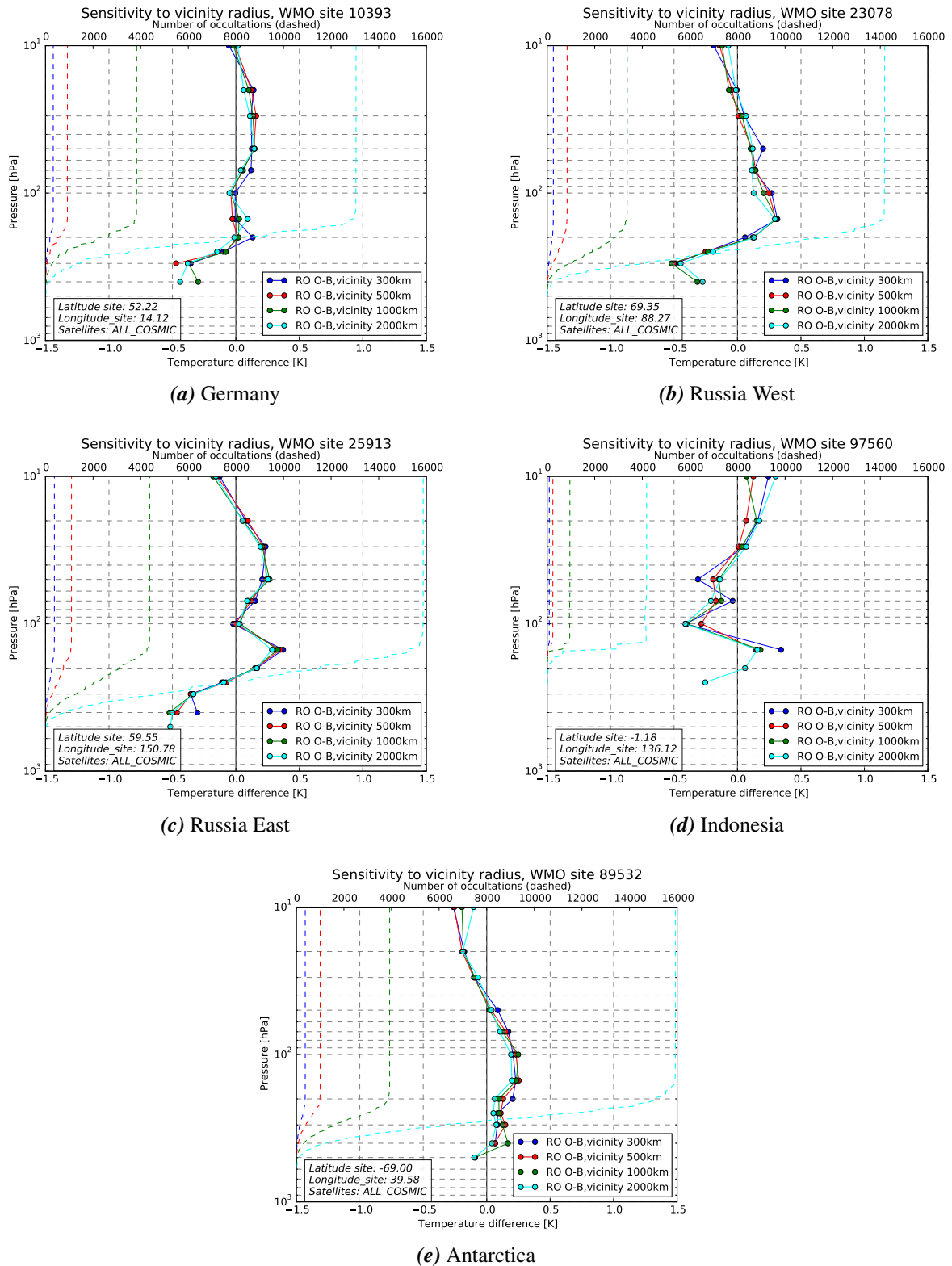


**Figure 4.8:** Sensitivity of the RO Tdry departure statistics to the vicinity radii for five example sites, see table 4.1. The dashed lines give the number of measurements used to calculate the statistics.

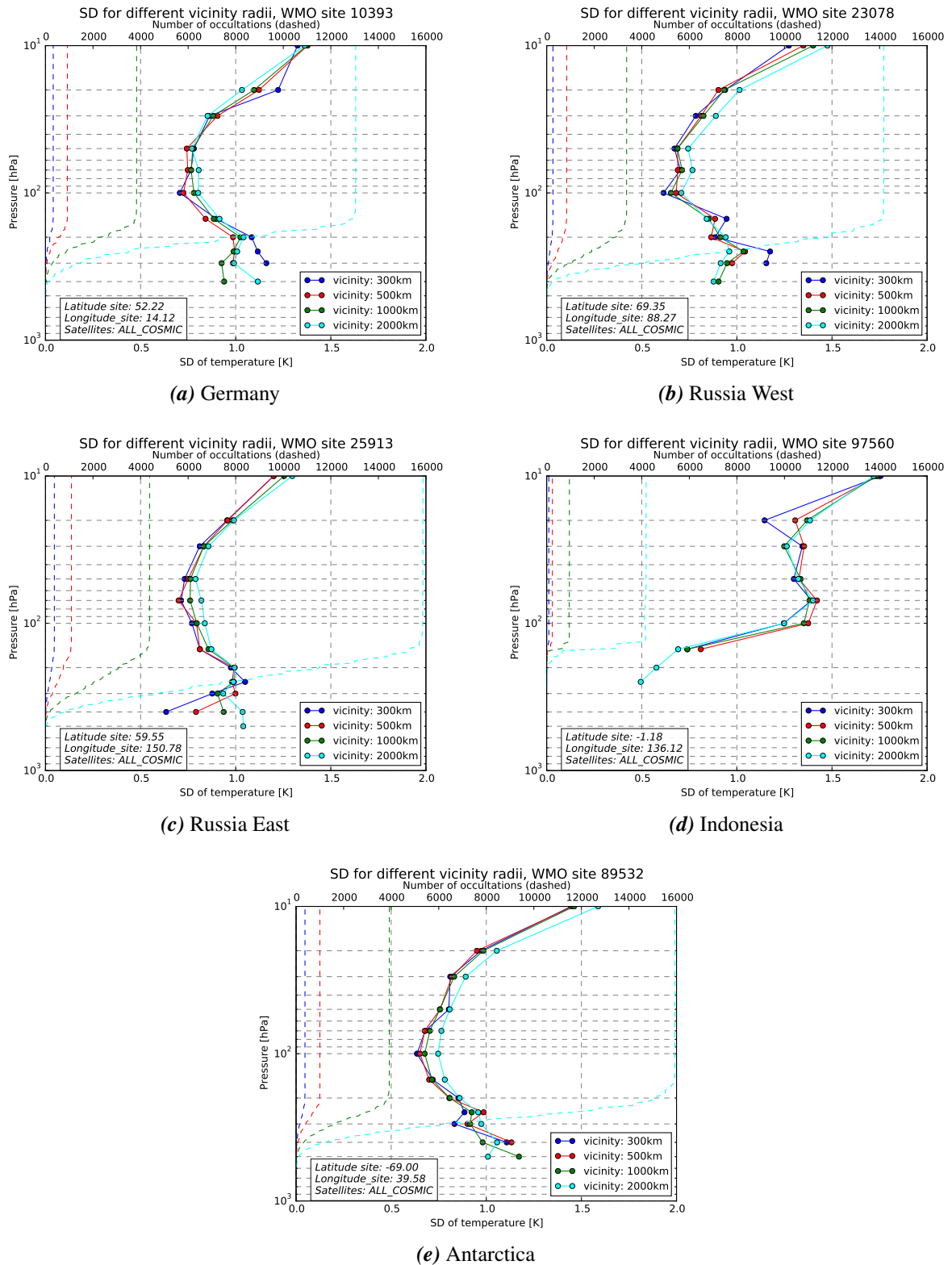


**Figure 4.9:** Sensitivity of the SD for RO Tdry departure statistics to the vicinity radii for five example sites, see table 4.1. The dashed lines give the number of measurements used to calculate the statistics.

## 4.4 Rising and setting occultations

The RO technique enables rising and setting RO events, i.e. if the GNSS satellite rises from behind the horizon seen from the viewpoint of the low earth orbit satellite, which receives the signal, it is a rising occultation. The influence of solely using either rising or setting occultations to produce the mean departures is expected to be small in the stratosphere, given an adequate sample size. In the troposphere, reliable measurements are more difficult to obtain for rising occultations. The comparison of the departure statistics for rising and setting occultations can also be used as a quality check for the retrieval, where small differences indicate a good retrieval.

Figures 4.10 and 4.11 show the differences between the mean RO Tdry departures for the use of only rising (red), only setting (green) and all ROs (blue). Panels (a) to (d) show the results for different vicinity radii from 300 km to 2000 km. For the upper-air site in Germany (figure 4.10), given a vicinity radius of 300 km there are considerable differences between the statistics using only rising or setting ROs, but this difference decreases with increasing sample size, which is caused by enlargement of the vicinity radius. For the Indonesian site, where the sample size is comparably small, the differences are bigger for both 300 km and 500 km vicinity radii. This will be due to the small sample sizes; the differences nearly vanish when increasing the vicinity radii. Since the sensitivity study shows that the dependence on using entirely rising or setting occultations is vanishing given an appropriate sample size, this study uses both rising and setting occultations to diagnose radiosonde temperature biases.

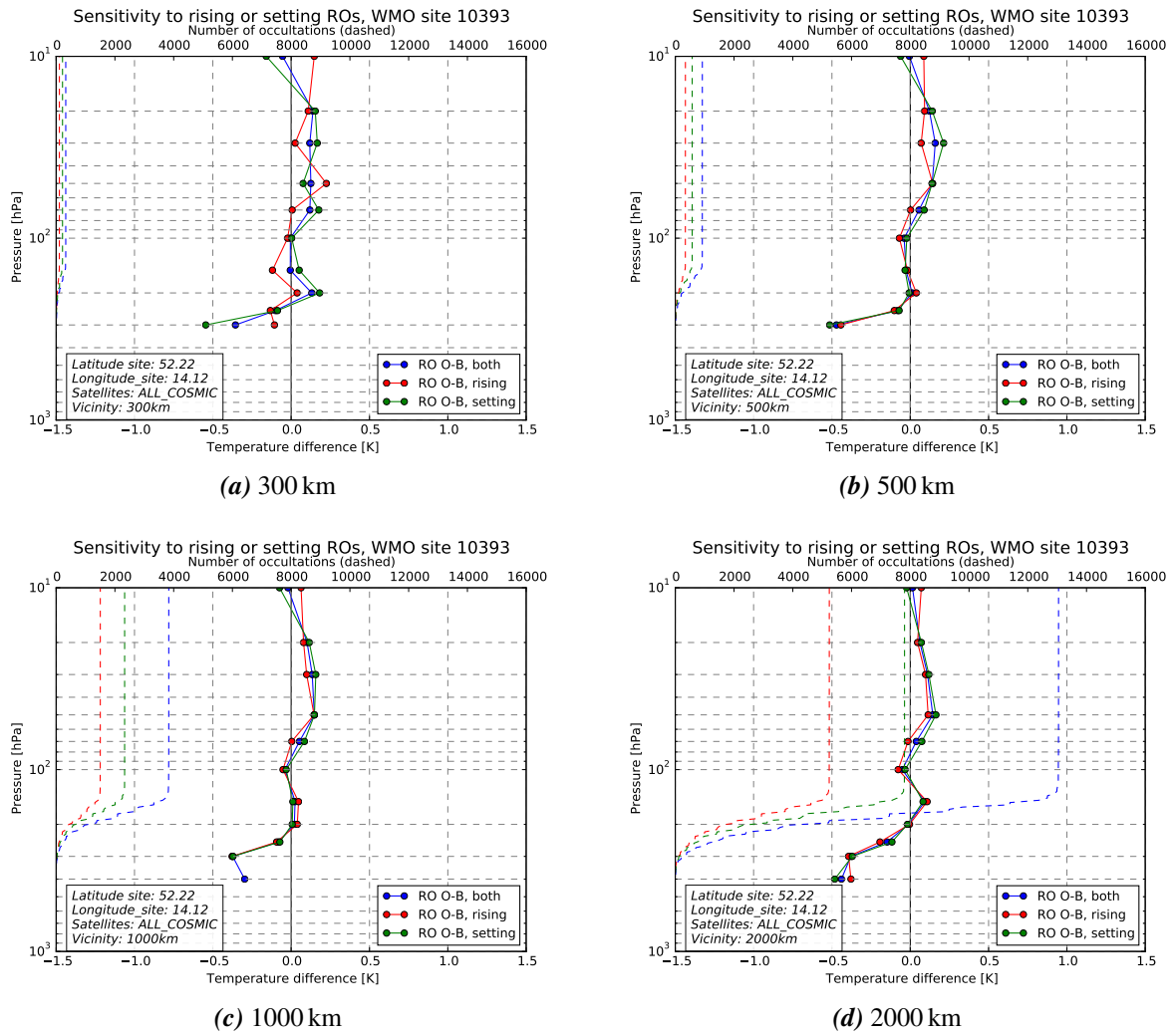


**Figure 4.10:** Sensitivity to the use of rising or setting occultations for different vicinity radii, WMO site 10393 in Germany.

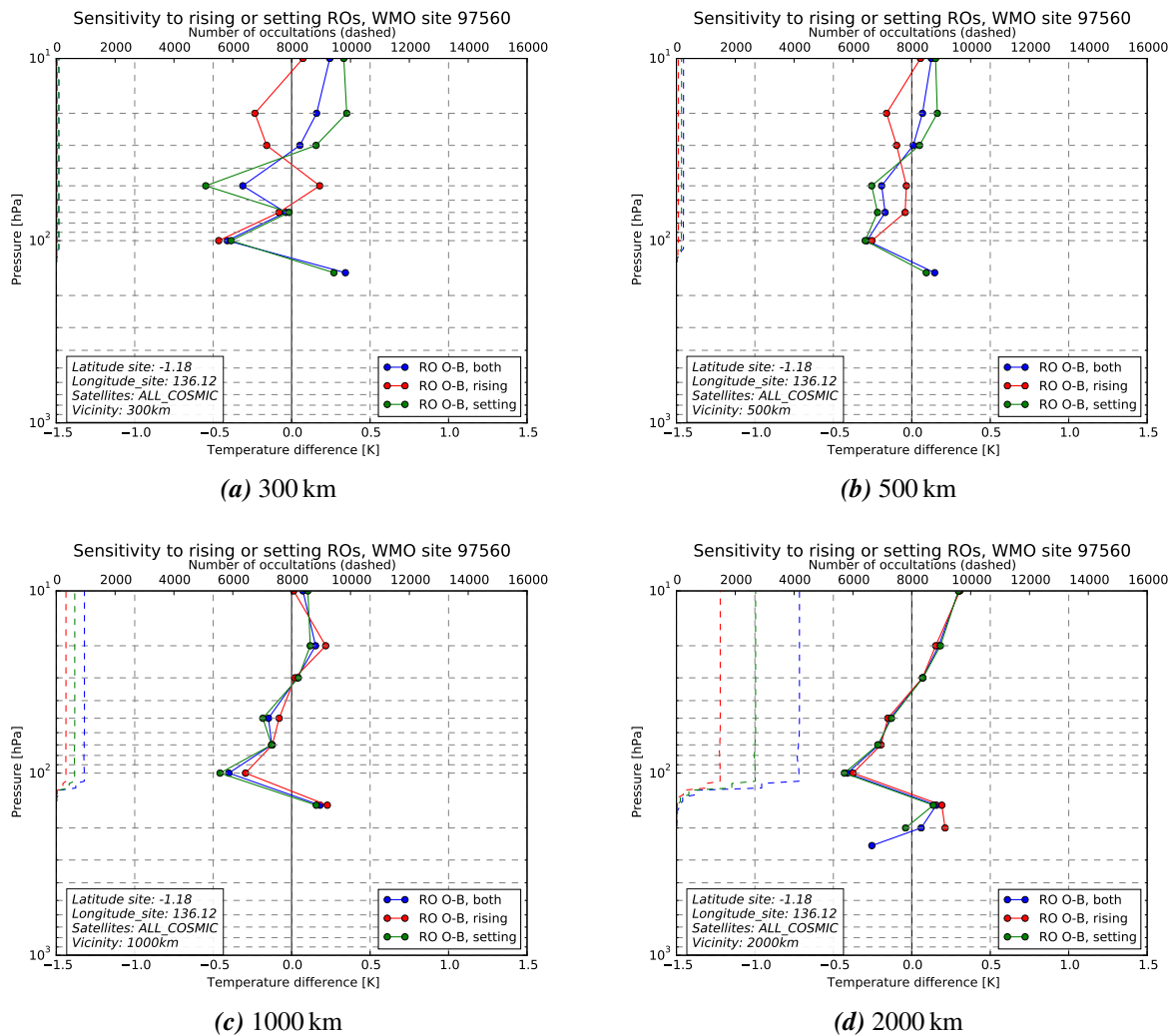


**Figure 4.11:** Sensitivity to the use of rising or setting occultations for different vicinity radii, WMO site 97560 in Indonesia.

## 4.5 Solar elevation angle

### 4.5.1 Radio occultation

The signal transmitted by the GNSS satellite traverses not only the neutral atmosphere, but also the ionosphere, which contains charged particles. While the ionospheric influence is corrected for in RO retrievals, it is still possible to have an influence caused by the ionosphere which depends on the SEA. Four different SEA ranges are analysed here to investigate the influence of the position of the sun on the RO measurements.

Name	SEA range [degree]
High	SEA > 22.5°
Low	7.5° < SEA < 22.5°
Dusk	-7.5° < SEA < 7.5°
Night	SEA < -7.5°

**Table 4.2:** Solar elevation angle ranges.

The effect of the SEA on the mean RO Tdry departures is shown in the figure 4.12 for different vicinity radii.

The influence of the SEA on the Tdry departures is most distinct for low vicinity radii, but it also does not vanish for large vicinity radii, where the Tdry departures for high solar elevation angle show a considerable difference compared to the other SEAs. The differences in the Tdry departures cannot reliably be attributed to the dependence of the RO observations to the SEA, as the model state may have a diurnal bias and therefore could cause the dependence on the SEA range. Based on these results the study will divide the RO profiles into the four SEA ranges shown in table 4.2.

#### 4.5.2 Radiosonde

The RS temperature biases depend on the solar elevation, as can be seen in Philipona et al. [23], Sun et al. [32], Dirksen et al. [5]. While the solar radiation can cause a positive temperature bias during daytime, negative biases due to thermal emission are usual during nighttime. Therefore the RS data set is divided into the same SEA angle ranges as the RO dataset. Subdividing both datasets based on the SEA also helps to accounts for possible SEA dependent biases in the model background, since both measurement types are compared against the background in the same SEA.

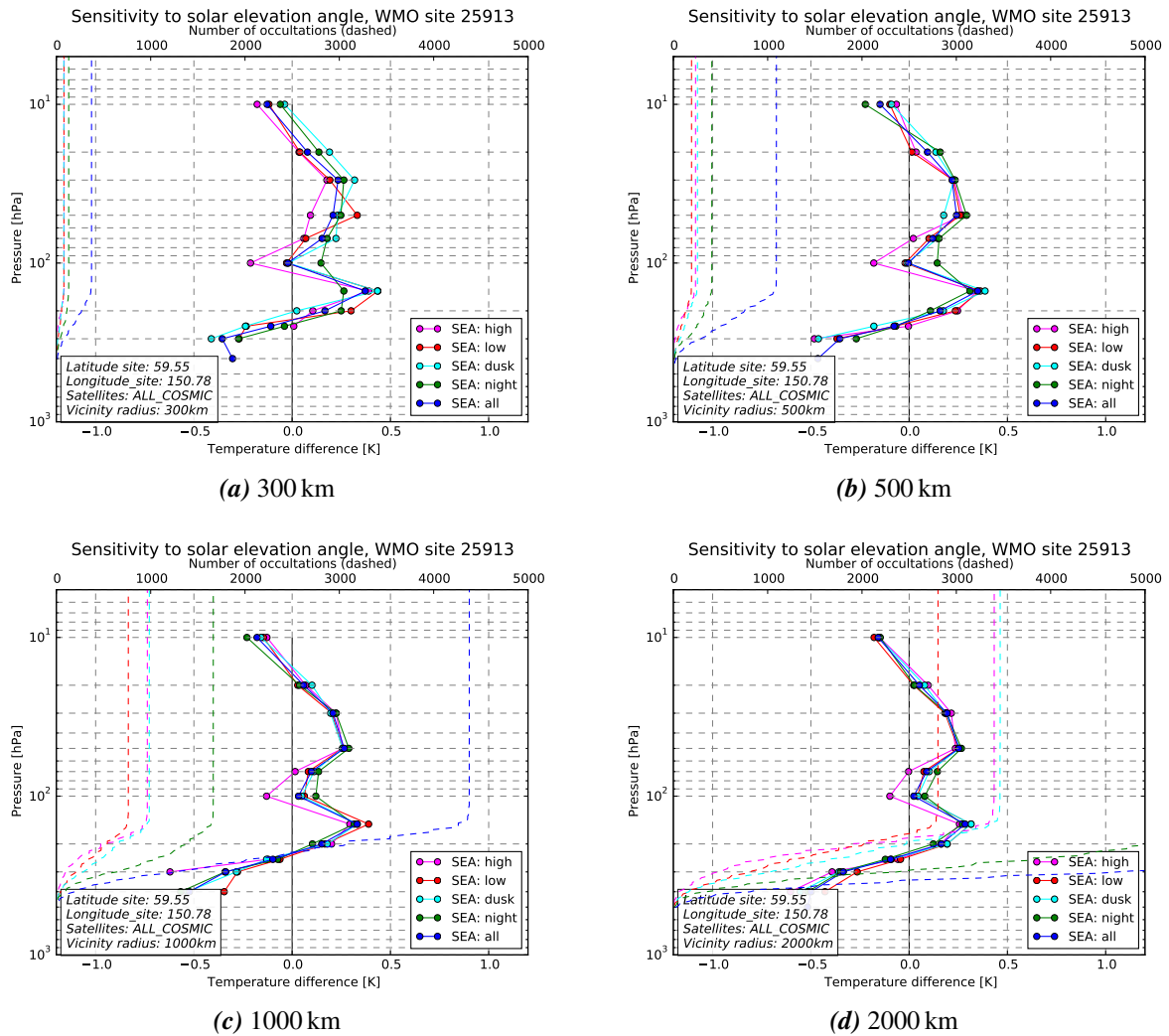


**Figure 4.12:** The sensitivity of RO Tdry departures to solar elevation angle for different vicinity radii, WMO site 25913 in Russia.

## 4.6 Different RO missions

To use a combined statistic of RO BA data from various missions, the homogeneity of the different missions needs to be tested. If the departure statistics depend on the RO mission, a correction of the bias between the missions is needed before they are combined.

Here we analyse the difference in the COSMIC and GRAS departure statistics for the Russian station in figure 4.13, where the vicinity radius and thereby the sample size is increased from (a) to (d). Although the differences in the departures statistics get smaller with an increasing vicinity radius, they do not completely vanish. For most of the example stations from table 4.1, the results are similar (figures not shown), though the differences are considerably larger for the Indonesian site, although more than 1000 profiles of COSMIC and GRAS combined exist.

The difference in the departure statistics between COMIC and GRAS could inter alia be caused by the different times when the measurements are taken. GRAS passes a given place

at the same local time every day, while the COSMIC profiles comprise all daytimes. Although the dependence of RO measurement on the time of the day is small, also the model might have a diurnal bias, that has an effect in the departure statistics.

Since the different RO missions have an influence on the departure statistics, this study concentrates on the COSMIC RO BA profiles. For operational implementation a more detailed study about how to combine the different missions to calculate the Tdry departures should be conducted in order to allow statistics to be produced using, for example, data from a few months rather than an entire year.

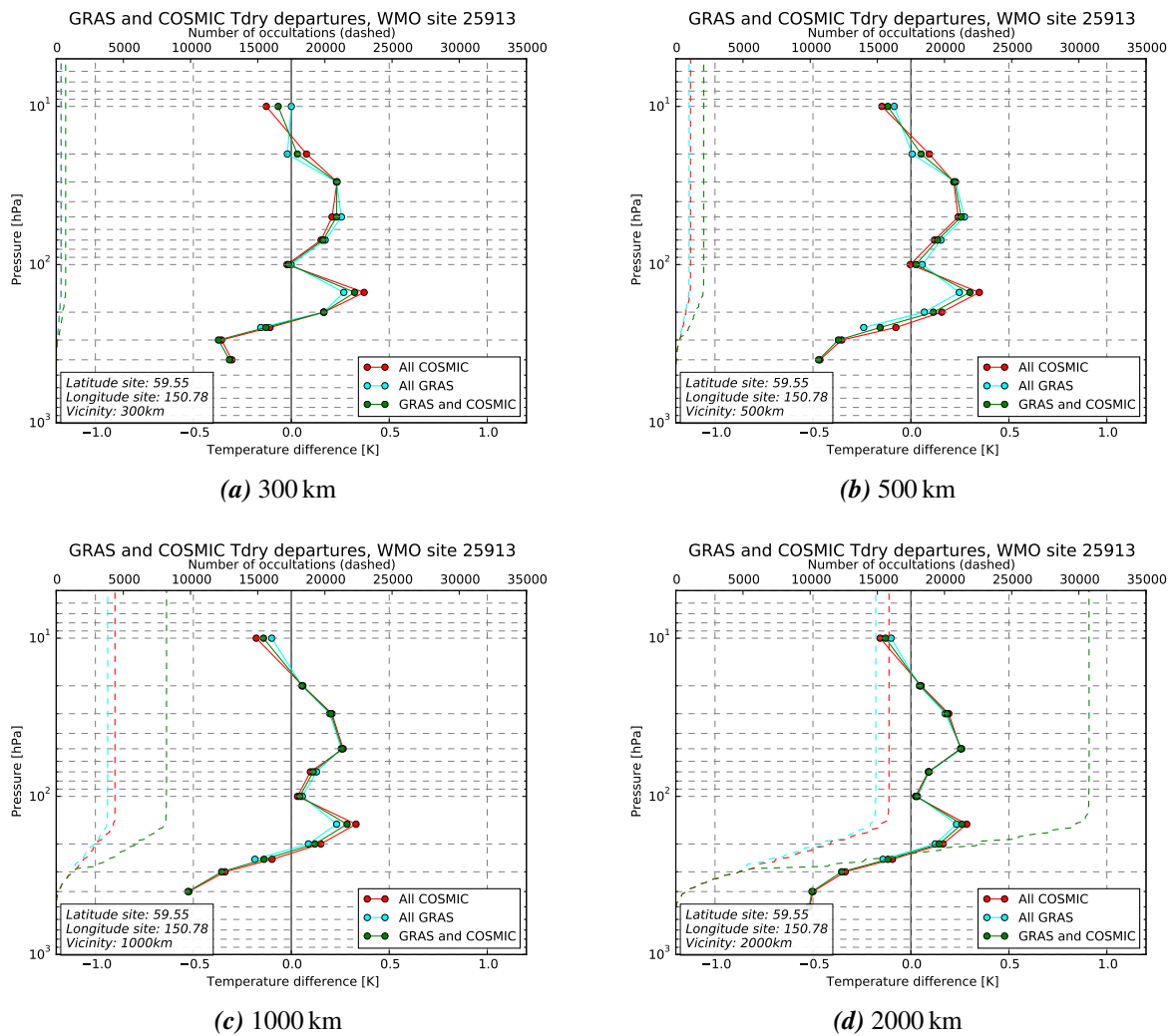


**Figure 4.13:** The influence of using different RO missions to calculate the Tdry departure statistics for the East Russia example site. All COSMIC satellites (red), all GRAS satellites (GRAS-A and GRAS-B) (cyan), all COSMIC and all GRAS combined (green).

## 5 Comparison of departure statistics for RS and RO

In this chapter the RO and RS departures are compared and the bias correction is presented for the example upper-air sites in table 4.1. The difference between the mean departure, calculated for both instruments, can be used as an estimate of the temperature bias in the RS profile. Due to the high accuracy of RO measurements (see Anthes [1]), they are assumed to be an unbiased reference in this study. We aim to calculate the RS bias separately for every RS launch site and thus are not making a statement about the bias characteristics of certain RS types.

Figures 5.1 to 5.5 show the RO Tdry departures (blue), the RS temperature departures (red) and the bias correction (green, the bias correction is shown in the plots, identical to bias but opposite sign) on standard pressure levels for different SEA as defined in table 4.2. The dashed red and blue lines give the number of measurements used to calculate the statistics for RS and RO respectively. The RS types that are used most commonly at the respective site are given as a number in the bottom left corner of the plots and a list of the RS types can be found in the table B.1. The black dashed line gives the RS temperature after a the so-called “Hawson” correction, which is based on Hawson and Caton [9], was applied. The correction is only used at some stations and gets updated regularly. The correction plotted here is based on the values that were used in the operational system in August 2015, thus they might not agree with the corrections applied in 2014. The Hawson correction exists separately for the 12 UTC and 00 UTC launch time and is unchanged within three hours of 12 UTC and 00 UTC respectively. For all other observation times the correction is interpolated to the launch time. If no Hawson correction is used the black dashed line is on top of the red line for the RS departures.

The bias corrections calculated in this project are based on the RS temperature profile as submitted by the upper-air site. This implies that the profiles might be corrected by the RS manufacturer at the ground station, but no other correction scheme is used, in particular no Hawson correction is applied to the RS profiles that are used to build the statistics in this study.

The lowest level at which the RO Tdry departures, and hence RS bias corrections, are calculated depends on the amount of moisture at different levels in the atmosphere. At the Antarctic upper-air site (figure 5.5) a bias correction down to 400 hPa is calculated for both dusk and nighttime launches, though the SE at 400 hPa is fairly large due to the small number of RO BA profiles used to calculate the statistics. At the Indonesian station, see figure 5.4, the bias correction is only calculated from 10 hPa down to 100 hPa because the humidity is too high to analyse dry temperatures at lower levels. Furthermore, at this station a bias correction is not calculated for all SEA ranges, since there were no launches in the low and dusk SEA range. Importantly, as the RO Tdry departures at the lowest levels might be calculated from a subset of ROs (see blue dashed line for RO sample size), which is sampled in especially dry conditions, the calculated bias corrections might not be representative for all atmospheric conditions.

From the five example sites shown here, the RS temperature biases are smallest at the German site, which uses a Vaisala RS92 sonde and at the Antarctic station using Meisei sondes. While our estimation of the bias at the German example site agrees well with the estimation in Ladstädter et al. [19] at the highest level, we find a slight negative bias between  $\approx 200$ -

30 hPa, which is not obvious in Ladstädter et al. [19], who analysed the differences in RS and RO for the years 2002-2013. The differences might be caused by the choice of analysed years, as the vendor correction in the RS92 profiles might have changed. Furthermore, as described in section 3.2, RS92 TEMP profiles are almost 0.15 K to cold in the Met Office global NWP system, which partly explains the negative bias found in our analysis.

Although the Indonesian site (Fig. 5.4) launches Meisei sondes like the Antarctic example site, the bias corrections are larger, reaching about 1.3 K. This indicates that the RS bias/bias correction does not solely depend on the RS type (see also Milan and Haimberger [22]), but also on the station, possibly related to varying ground station software and different climate regimes (Sun et al. [32] analyses the RS bias for different latitude bands). This finding supports our approach to calculate the bias correction on a station-by-station basis rather than based on the RS type.

At the two Russian upper-air stations a variety of RS types was launched during 2014, but only the main types are listed in the figures (more details available in table 4.1). While the RS bias correction at the site in western Russia (Fig. 5.2) stays below 0.7 K for “dusk” and “night” and is only larger at the highest level for “high” and “low” SEAs, a larger bias correction is needed at the site in eastern Russia (Fig. 5.3). Here, the bias correction is largest for “dusk” and “night”, reaching values up to about 2.5 K. Interestingly no Hawson bias correction is performed at this station, while the RS temperature profile at the West Russian station is Hawson-corrected, which actually increases the difference between RS and RO. The reason for this is not clear, but it could be because the Hawson correction as used here is from August 2015. Although this is an inconsistency in the data, it does not affect the calculated bias correction, but only the Hawson corrected temperature plotted for comparisons.

Interestingly the RS temperatures at many Russian sites show cold biases at all SEAs, leading to a positive bias correction at most levels. This is in contrast with the theoretical expected radiation bias, i.e. a warm bias during daytime and a cold bias during nighttime. Our results, however, agree with the findings by Rennie [25] for RS tracked with the Russian AVK radar. The cold bias that prevails for all SEAs could be caused by the correction of biases in the ground system software. In general, the raw RS profiles are not disseminated, but rather vendor-corrected profiles, for which the applied corrections are seldom traceable.

The temperature bias is calculated here on a station-by-station basis, disregarding which type of sonde and how many different sonde types are launched. This is a compromise made to achieve a sufficient sample size for statistical significance, given the other choices made to select the data. Though it might lead to problems for individual cases, e.g. if a site is launching a sonde with a bias characteristic, that is very different from the bias correction applied at the site, we expect that applying the bias correction operationally will improve the RS temperature profiles on average. This method would also allow to correct the temperature profile for launches where the sonde type is not submitted to the GTS. The SE of the RS departure profile gives an indication of the spread in the O-B statistics. A station which launches RS types with quite different biases, will have a larger SE in the departures and hence in the calculated temperature bias correction.

A RS temperature bias correction, as presented here for some example stations, has been calculated for 762 upper-air sites based on the departure statistics for 2014 and is available online at [http://www.romsaf.org/visiting\\_scientist.php#y2015](http://www.romsaf.org/visiting_scientist.php#y2015), though the Hawson corrected profile is excluded from these figures.

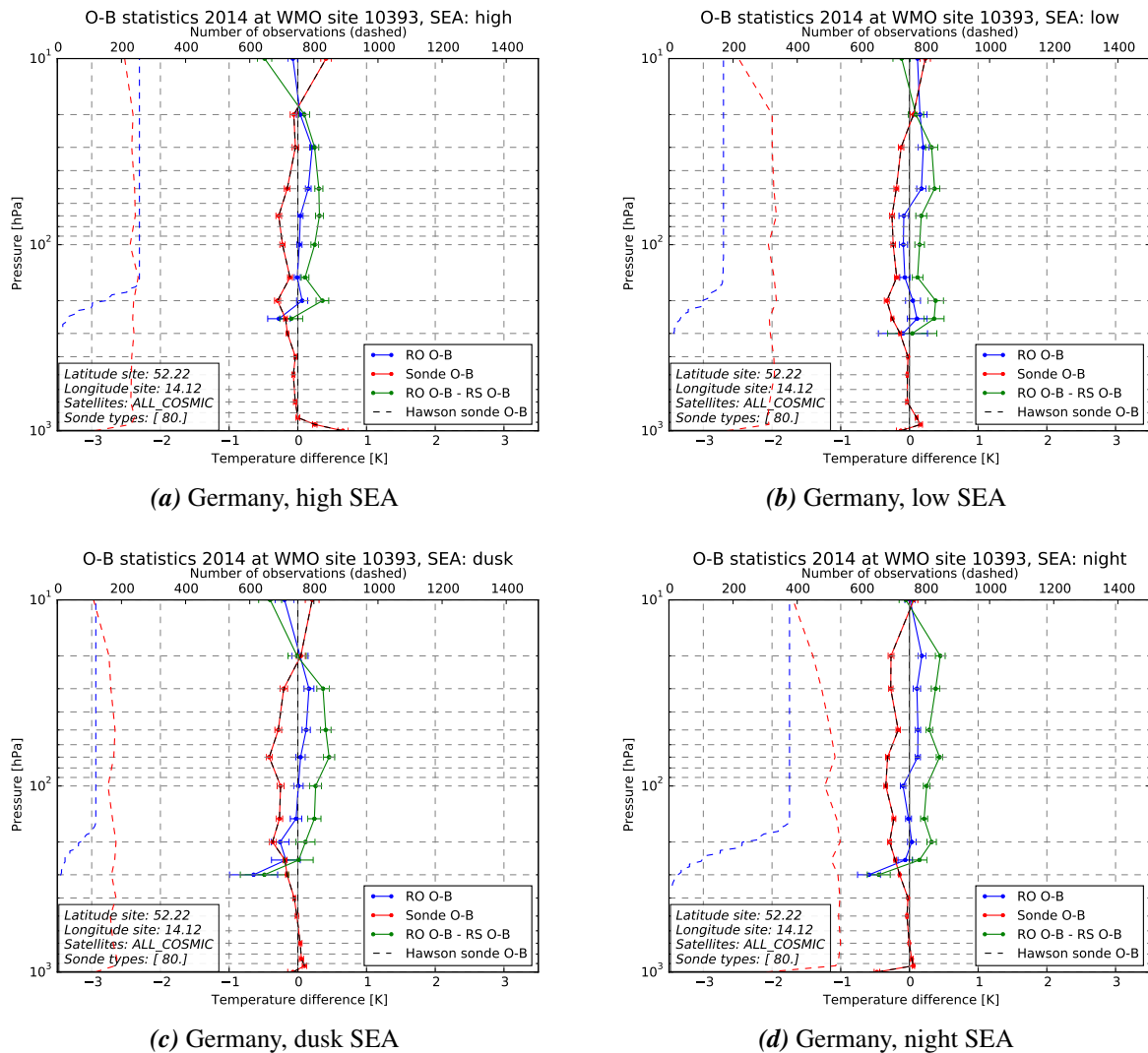
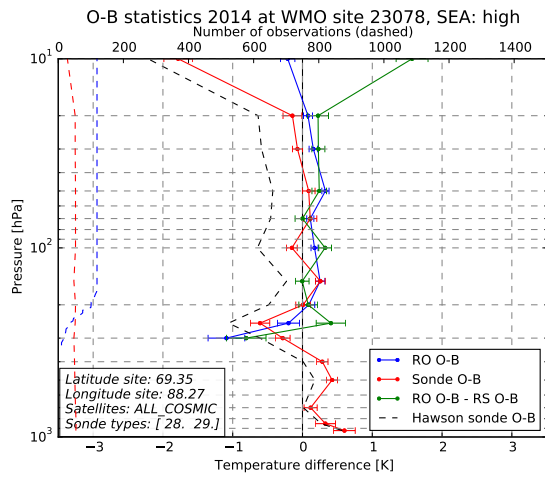
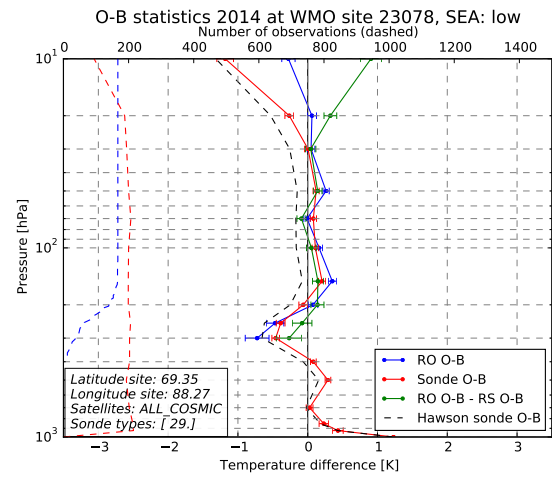


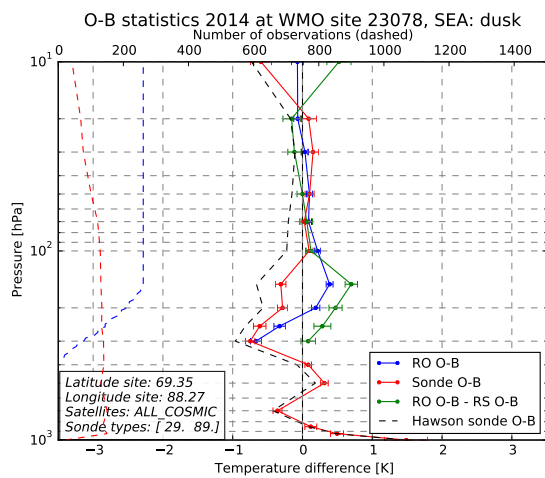
**Figure 5.1:** RO Tdry departure (blue), RS temperature departures (red) and bias correction (green) at the German example site for different SEA ranges (a)-(d). The Hawson corrected temperature (black dashed line on top of red line) is identical to the RS temperature, i.e. no Hawson correction applied.



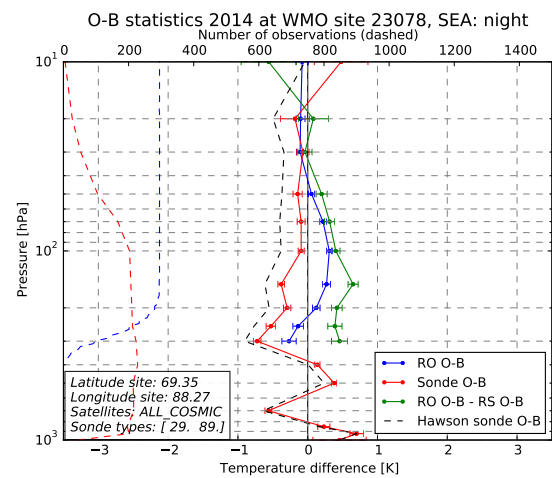
(a) Russia West, high SEA



(b) Russia West, low SEA

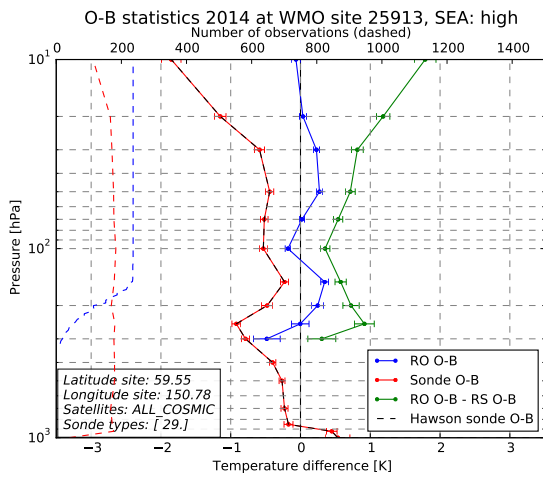


(c) Russia West, dusk SEA

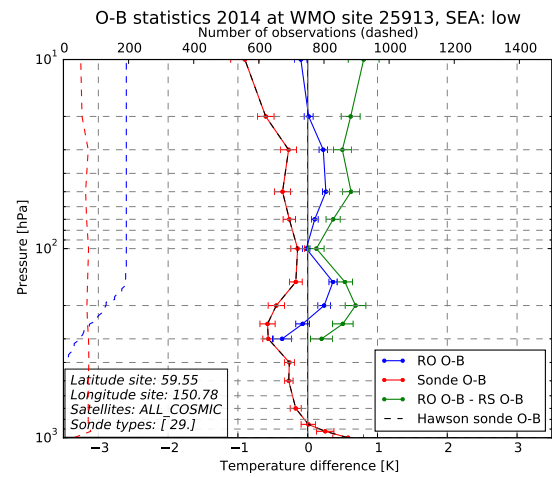


(d) Russia West, night SEA

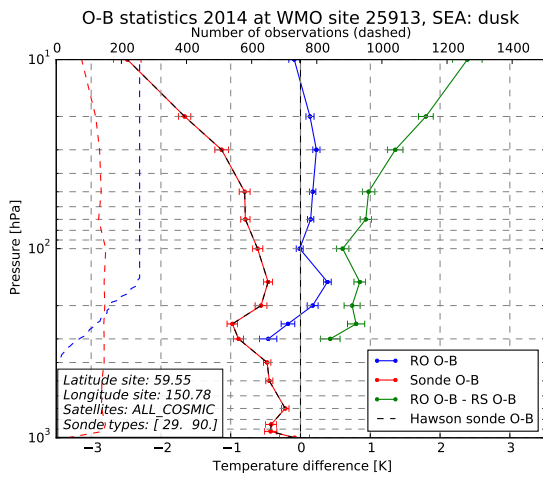
**Figure 5.2:** RO Tdry departure (blue), RS temperature departures (red) and bias correction (green) at the West Russian example site for different SEA ranges (a)-(d). The Hawson corrected temperature is shown as the black dashed line.



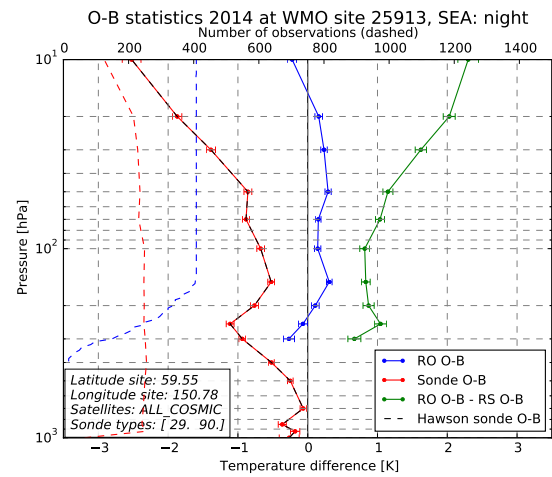
(a) East Russia, high SEA



(b) East Russia, low SEA



(c) East Russia, dusk SEA



(d) East Russia, night SEA

**Figure 5.3:** RO Tdry departure (blue), RS temperature departures (red) and bias correction (green) at the East Russian example site for different SEA ranges (a)-(d). The Hawson corrected temperature (black dashed line on top of red line) is identical to the RS temperature, i.e. no Hawson correction applied.

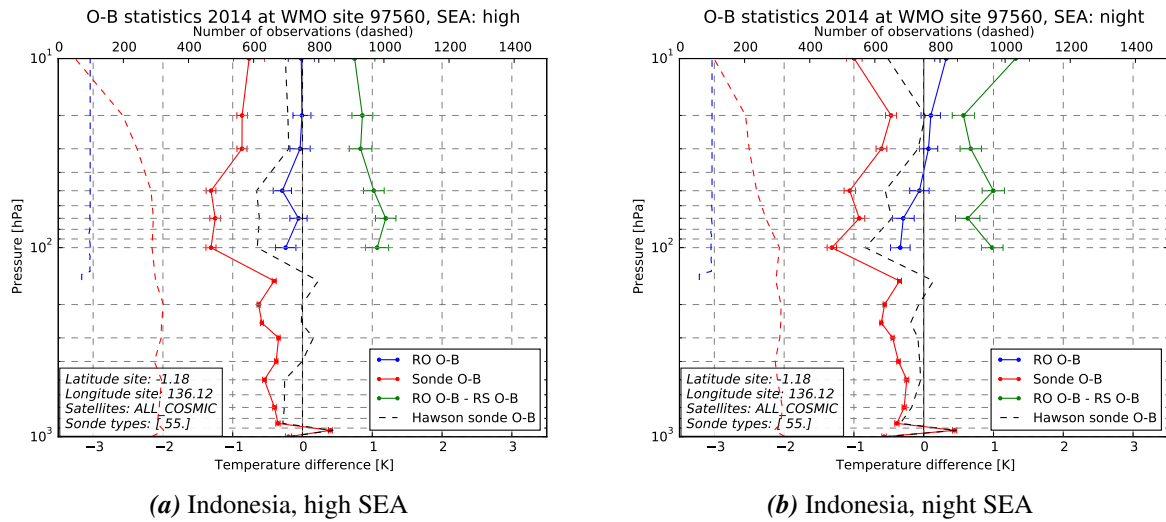


**Figure 5.4:** RO Tdry departure (blue), RS temperature departures (red) and bias correction (green) at the Indonesian example site for different SEA ranges (a)-(b). The Hawson corrected temperature is shown as the black dashed line.

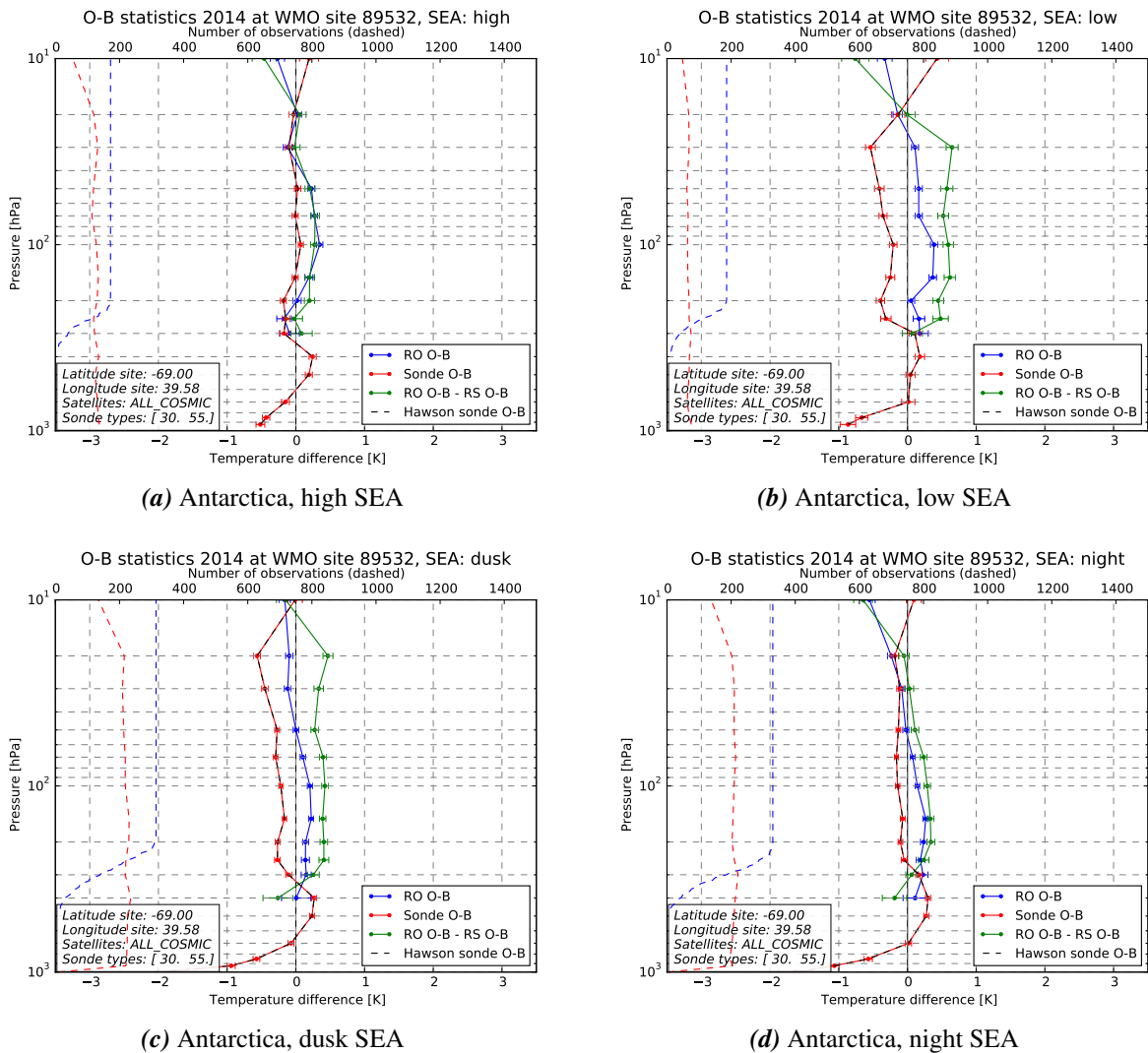


**Figure 5.5:** RO Tdry departure (blue), RS temperature departures (red) and bias correction (green) at the Antarctic example site for different SEA ranges (a)-(d). The Hawson corrected temperature (black dashed line on top of red line) is identical to the RS temperature, i.e. no Hawson correction applied.

## 6 Conclusions

A method to estimate the RS temperature bias on standard pressure levels based on a double differencing approach of RS and RO background departure statistics is presented and the bias corrections are shown for five carefully chosen example sites.

First, RS departure statistics at a site are calculated as the mean difference between the RS temperature and the NWP system background temperature. Similarly, the RO Tdry departure statistics, including all profiles within 500 km of the launch site are calculated (using the BA departures). Then, the difference between the RO and RS departure statistics (RO O-B minus RS O-B) estimates the temperature bias correction to be applied to RS temperature profiles, thus using the RO measurement as an unbiased reference. The NWP system serves as a transfer medium and diminishes the differences caused by imperfect co-location. The approach is based on the assumption that the bias in the NWP system does not vary within the vicinity radius of 500 km. Compared to the assumption of a non-varying atmosphere, which is used for direct observation-to-observation co-locations, this assumption is less severe and leads to relatively small SDs.

The double differencing technique has four advantages: (i) compared to direct RO to RS co-locations, the influence of differences in time and space is minimized, (ii) model humidity information allows determination of the lowest level where RO Tdry can be used, (iii) it is possible to use a TL retrieval of Tdry departures from RO BA departures which reduces the sensitivity to a priori information and (iv) the SE of the calculated bias correction is comparable low.

The applied tangent linear version of the Tdry calculation is described here for the first time. It is based on the linear Tdry calculation developed by Syndergaard [34], but differs in the details. In contrast to the non-linear calculation of Tdry profiles from BA profiles, the TL version calculates Tdry departures from BA departures. Thus the TL version enables a temperature departure to be computed from any subset of a BA departure profile (see section 4.2). Analysing the Tdry departures and covariance matrices for different upper impact height cut-offs reveals that not only the Tdry departures, but also the covariance of the Tdry departures depend on the choice of upper impact height cut-off. Thus, determining this upper cut-off is a crucial part of this research project. Based on the scope of the study and the investigation of covariances, an impact height of 35 km is chosen as the upper threshold. The BA departures above the threshold are set to zero to eliminate the effect of model biases and a priori information in the higher levels.

Some pragmatic decisions are needed to calculate the RS temperature bias based on RO and RS departures. Therefore a sensitivity study has been performed to determine the final set-up for the analysis. The RS temperature bias strongly depends on the position of the sun and therefore the RS and RO departures and bias corrections are also calculated separately for four different SEA ranges, namely 'high' ( $SEA > 22.5^\circ$ ), 'low' ( $7.5^\circ < SEA < 22.5^\circ$ ), 'dusk/dawn' ( $-7.5^\circ < SEA < 7.5^\circ$ ) and 'night' ( $SEA < -7.5^\circ$ ). Increasing the radius around the upper-air site, in which the RO profiles are used to calculate the mean Tdry departures, has a minor effect on the O-B statistics. Radii of 300 km, 500 km, 1000 km and 2000 km are tested and a radius of 500 km is chosen for this study. The difference between using entirely rising or setting occultation in the RO Tdry departure calculation becomes negligible given an adequate sample size and thus all occultations are used. A comparison of the RO

Tdry departures using either COSMIC, GRAS, or the occultations from both missions combined, highlights differences that, although small, do not vanish with increasing sample size. Therefore this study uses COSMIC occultations only. A homogenisation of the two data sets, which show different departures statistics, might be needed before both can be combined to study RS temperature biases. For operational use this is strongly encouraged to enlarge the sample size.

The RO and RS departures, their respective SEs and the temperature bias corrections, calculated as the difference between the RO and RS departures, are analysed. Also, the SE of the temperature bias correction, which is an essential part of results, is computed. The SE of the bias allows a decision to be made as to whether a correction of the RS temperature should be performed or not, e.g. for certain sondes, the RS temperature on certain pressure levels might be within the SE range of the temperature bias.

The temperature bias correction and its SE is calculated for most upper-air stations launching RS that submitted data to the Global Telecommunication System in 2014. The bias correction is calculated separately for different SEA. Depending on the amount of daily launches and the local launch time, a correction for all SEA ranges, or for a subset of them is calculated plots are available to at [http://www.romsaf.org/visiting\\_scientist.php#y2015](http://www.romsaf.org/visiting_scientist.php#y2015).

A positive RS temperature bias is theoretically expected during daytime from solar irradiance, while the emission of radiation by the RS can cause a negative bias during nighttime. Most RS manufacturers account for these biases in the ground station software and disseminate a corrected RS profile. Such corrected profiles are analysed here, which might explain why the sign of the bias does not always agree with the expectation based on theory. This is especially obvious for Russian upper-air sites where the temperature bias tends to be negative for all SEA ranges and can exceed -2 K at the 10 hPa level.

Depending on the station, the RS type and the SEA, the magnitude of the bias varies. For some stations the estimated temperature bias stays below 0.5 K throughout the whole profile, while it exceeds 2 K at others stations. An increase of the bias with increasing altitude is found for many stations, especially those that show large biases. Sites launching the Vaisala RS92 sonde, which is often used as reference, tend to show a small negative bias in the lower levels and a positive bias in the highest level during daytime and a slightly negative bias at most levels during nighttime. Though, the RS92 TEMP profile has a 0.15 K cold bias in the Met Office NWP system (Ingleby and Edwards [15]) which makes the calculated correction dependent on the NWP system. However, the bias is calculated for each upper-air site separately and differences in the bias characteristic occur even if the same sonde type is launched, as was also found by Milan and Haimberger [22]. This can be caused, for example, by different versions of the vendor software.

The technique presented here could be implemented in NWP systems to correct RS temperature biases before the profiles are assimilated. For each observed RS profile, the bias correction for the corresponding site and SEA would be interpolated onto the observation levels (with values extended below the lowest valid correction). The interpolated bias correction can then be added to the observed temperatures prior to assimilation. A forecast impact study of such an experiment is planned using the Met Office global NWP system.

In operational weather forecasts, the bias correction presented here could be calculated on a regular basis, e.g. every month, where the influence of single departures in the departure statistics would decrease going further into the past, i.e. highest weight will be given to recent observations. The bias correction could then be applied before the RS temperature profiles

are assimilated into the model. It could replace the Hawson correction (Hawson and Caton [9]) that is currently applied for some RS stations. The correction of RS temperatures prior to assimilation should serve the need for consistent measurements to anchor NWP models. Assimilating inconsistent temperature profiles may lead to false horizontal temperature gradients, generating spurious features in the wind field. Thus, a consistent set of RS and RO profiles has the potential to improve the NWP.

This report not only shows the potential of RO measurements to correct the biases in other observation types, but also the advantages of using a tangent linear calculation of Tdry departures based on the RO BA departures. Thus this research project can serve three main user groups, (i) a bias correction for RS temperatures is produced serving the RS community, (ii) the method is explained to serve the data assimilation and NWP community, who can implement the technique operationally and (iii) the new tangent linear version of the linear Abel transform and the hydrostatic integration is provided to the RO community.

This analysis was performed as a ROM SAF Visiting Scientist project during September and October 2015 and due to the short time frame some questions will need to be answered in future research projects. To estimate the effect of applying the bias correction suggested here, a forecast impact study is planned. Since RO Tdry profiles, and with it the bias correction calculated here, are only available in the stratosphere down to an altitude where humidity starts to become significant, a pragmatic decision about the correction of the RS temperature in the troposphere is needed. Either a linear decrease of the bias below the lowest level at which the bias is provided, or a bias correction based on the RS departures and some additional smoothing is conceivable and will be addressed in the ongoing work.

Furthermore it is planned to analyse the reference-quality RS profiles from the GCOS (Global Climate Observing System) Reference Upper-Air Network (GRUAN, GCOS-112 [7]). This is possible for those GRUAN stations that do not only use the raw RS profile to calculate a GRUAN processed profile, but also submit the RS profiles as provided by the vendor software to the GTS. An example for such a GRUAN site is Lindenberg, Germany. If the RS profile is timely submitted to the GTS and is assimilated into the Met Office Unified model, a model background exists, which can then also be used to calculate the temperature departures for the GRUAN data product, which becomes available with some time delay and therefore is not assimilated in NWP models nowadays.

Also the vicinity radius which is chosen to be 500 km for all RS stations in this study could be improved in future studies by e.g. using the departure statistics to determine up to which distance data can be included. Increasing the vicinity radius would lead to a bigger sample size, but a too big vicinity radius could decrease the quality of the bias estimation. Depending on the station a different vicinity radius could be chosen based on the standard deviation of the departure statistics.

Moreover the influence of the upper impact height cut-off could be further investigated in a separate study. Here we show that the RO temperature departure statistics are highly influenced by the impact height above which the BA departures are set to zero. This result will also be of interest for other studies and should therefore be addressed in future work.

Prior to the preparation of version 2 of this report a paper covering the main outcomes from this project and some new results was submitted to the American Meteorological Society Journal of Applied Meteorology and Climatology. The title of the paper as submitted is "A new method to correct radiosonde temperature biases using radio occultation data".

## 6.1 Acknowledgements

This report is prepared in close collaboration with Chris Burrows, whom I can't thank enough for his help throughout the whole project, from the preparation and analysis of the data to writing the report. Furthermore I am very thankful to Sean Healy who provided the Tdry calculation and supported me throughout the project with many fruitful discussions. I would certainly like to thank John Eyre who developed the concept for this research project and discussed the results with me throughout the project. Furthermore I'm very thankful to Bruce Ingleby who provided helpful knowledge about radiosonde, Axel von Engelmann who did the final review of the report and supported me with useful comments and Sasha Kats who provided information about radiosonde types. I also like to express my gratitude towards the ROM SAF who provided the funding for this project and the German Academic Exchange Service who grants my PhD funding (DAAD-Doktorandenstipendium).

## Bibliography

- [1] Anthes, R. A. (2011). Exploring Earth's atmosphere with radio occultation: contributions to weather, climate and space weather. *Atmos. Meas. Tech.*, 4:1077–1103.
- [2] Burns, R. B. and Dobson, C. B. (1981). Standard error of the difference between means. In *Experimental Psychology Research Methods and Statistics*, pages 151–157. Springer Verlag.
- [3] Burrows, C. P., Healy, S. B., and Culverwell, I. D. (2014). Improving the bias characteristics of the ROPP refractivity and bending angle operators. *Atmos. Meas. Tech.*, 7:3445–3458.
- [4] Davies, T., Cullen, M. J. P., Malcolm, A. J., Mawson, M. H., Staniforth, A., White, A. A., and Wood, N. (2005). A new dynamical core for the Met Office's global and regional modelling of the atmosphere. *Quart. J. Roy. Meteor. Soc.*, 131:1759–1782.
- [5] Dirksen, R. J., Sommer, M., Immler, F. J., Hurst, D. F., Kivi, R., and Vömel, H. (2014). Reference quality upper-air measurements: GRUAN data processing for the Vaisala RS92 radiosonde. *Atmos. Meas. Tech.*, 7:4463–4490.
- [6] Fjeldbo, G., Kliore, A. J., and Eshleman, V. R. (1971). The neutral atmosphere of Venus as Studied with the Mariner V Radio Occultation Experiments. *The Astronomical Journal*, 76(2):123–140.
- [7] GCOS-112 (2007). GCOS Reference Upper-air Network (GRUAN): Justification, requirements, siting and instrumentation options. Technical report. WMO/TD No.1379.
- [8] Haimberger, L., Tavolato, C., and Sperka, S. (2012). Homogenization of the Global Radiosonde Temperature Dataset through Combined Comparison with Reanalysis Background Series and Neighboring Stations. *J. Climate*, 25:8108–3131.
- [9] Hawson, C. L. and Caton, P. G. F. (1961). A synoptic method for the international comparison of geopotential observations. *The Meteorological Magazine*, 90(1073):333–364.
- [10] He, W., Ho, S., Chen, H., Zhou, X., Hunt, D., and Kuo, Y.-H. (2009). Assessment of radiosonde temperature measurements in the upper troposphere and lower stratosphere using COSMIC radio occultation data. *Geophys. Res. Lett.*, 36.
- [11] Healy, S. B. (2008). Assimilation of GPS Radio Occultation Measurements at ECMWF. In *GRAS SAF Workshop on Applications of GPSRO Measurements, 16-18 June 2008*, pages 99–109, ECMWF, Shinfield Park, Reading, UK. European Centre for Medium-Range Weather Forecasts. available at [http://www.romsaf.org/Workshops/agrom\\_prog/Healy.pdf](http://www.romsaf.org/Workshops/agrom_prog/Healy.pdf).
- [12] Healy, S. B. and Culverwell, I. D. (2015). A modification to the standard ionospheric correction method used in GPS radio occultation. *Atmos. Meas. Tech.*, 8:3385–3393.

- [13] Healy, S. B. and Thépaut, J.-N. (2006). Assimilation experiments with CHAMP GPS radio occultation measurements. *Quart. J. Roy. Meteor. Soc.*, 132:605–623.
- [14] Hoffman, R. N., Louis, J.-F., and Neerkorn, T. (1992). A method for implementing adjoint calculations in the discrete case. ECMWF Technical Memorandum 184.
- [15] Ingleby, B. and Edwards, D. (2015). Changes to radiosonde reports and their processing for numerical weather prediction. *Atmos. Sci. Let.*, 16:44–49.
- [16] Kobayashi, S., Ota, Y., Harada, Y., Ebata, A., Moriya, M., Honoda, H., Onogi, K., Kamahori, H., Kobayashi, C., Endo, H., Miyaoka, K., and Takahashi, K. (2015). The JRA-55 Reanalysis: General Specifications and Basic Characteristics. *J. Meteorol. Soc. Jpn.*, 93:5–48.
- [17] Kursinski, E. R., Hajj, G. A., Leroy, S. S., and Herman, B. (2000). The GPS Radio Occultation Technique. *Terrestrial, Atmospheric and Oceanic Sciences*, 11(1):53–114.
- [18] Kursinski, E. R., Hajj, G. A., Schofield, J. T., Linfield, R. P., and Hardy, K. R. (1997). Observing Earth's atmosphere with radio occultation measurements using the Global Positioning System. *J. Geophys. Res.*, 102:23429–23465.
- [19] Ladstädter, F., Steiner, A. K., Schwärz, M., and Kirchengast, G. (2015). Climate intercomparison of GPS radio occultation, RS90/92 radiosondes and GRUAN from 2002–2013. *Atmos. Meas. Tech.*, 8:1819–1834.
- [20] Leroy, S. S., Dykema, J. A., and Anderson, J. G. (2006). Climate Benchmarking Using GNSS Occultation. In Foelsche, U., Kirchengast, G., and Steiner, A., editors, *Atmosphere and Climate Studies by Occultation Methods*, pages 287–301. Springer-Verlag.
- [21] Leys, C., Ley, C., Klein, O., Bernard, P., and Licata, L. (2013). Detecting outliers: Do not use standard deviation around the mean, use absolute deviation around the median. *Journal of Experimental Social Psychology*, 49:764–766.
- [22] Milan, M. and Haimberger, L. (2015). Predictors and grouping for bias correction of radiosonde temperature observations. *J. Geophys. Res. Atmos.*, 120:10736–10766.
- [23] Philipona, R., Kräuchi, A., Romanens, G., Levrat, G., Ruppert, P., Brocard, E., Jeannet, P., Ruffieux, D., and Calpini, B. (2013). Solar and Thermal Radiation Errors on Upper-Air Radiosonde Temperature Measurements. *J. Atmos. Oceanic Technol.*, 30:2382–2392.
- [24] Poli, P., Healy, S. B., and Dee, D. P. (2010). Assimilation of Global Positioning System radio occultation data in the ECMWF ERA-Interim reanalysis. *Quart. J. Roy. Meteor. Soc.*, 136:1972–1990.
- [25] Rennie, M. P. (2010a). Investigation into the consistency of radiosonde and GPSRO observations and their application in NWP at the Met Office. Met Office Forecasting R&D Technical Report 541.
- [26] Rennie, M. P. (2010b). The impact of GPS radio occultation assimilation at the Met

Office. *Quart. J. Roy. Meteor. Soc.*, 136:116–131.

- [27] Rodgers, C. D. (2000). *Inverse methods for atmospheric sounding: Theory and practice*. World Scientific.
- [28] Scherllin-Pirscher, B., Kirchengast, G., Steiner, A. K., Kuo, Y.-H., , and Foelsche, U. (2011). Quantifying uncertainty in climatological fields from GPS radio occultation: an empirical-analytical error model. *Atmos. Meas. Tech.*, 4:2019–2034.
- [29] Simmons, A. J., Poli, P., Dee, D. P., Berrisford, P., Hersbach, H., Kobayashi, S., and Peubey, C. (2014). Estimating low-frequency variability and trends in atmospheric temperature using ERA-Interim. *Quart. J. Roy. Meteor. Soc.*, 140:329–353.
- [30] Smith, E. K. and Weintraub, S. (1953). The Constants in the Equation for Atmospheric Refractive Index at Radio Frequencies. *J. Res. Natl. Bur. Stand. (U. S.)*, 50(1):39–41.
- [31] Steiner, A. K., Kirchengast, G., and Ladreiter, H. P. (1999). Inversion, error analysis, and validation of GPS/MET occultation data. *Ann. Geophysicae*, 17:122–138.
- [32] Sun, B., Reale, A., Schroeder, S., Seidel, D. J., and Ballish, B. (2013). Toward improved corrections for radiation-induced biases in radiosonde temperature observations. *J. Geophys. Res.*, 118:4231–4243.
- [33] Sun, B., Reale, A., Seidel, D. J., and Hunt, D. C. (2010). Comparing radiosonde and COSMIC atmospheric profile data to quantify differences among radiosonde types and the effects of imperfect collocation on comparison statistics. *J. Geophys. Res.*, 115.
- [34] Syndergaard, S. (1999). Retrieval Analysis and Methodologies in Atmospheric Limb Sounding Using the GNSS Radio Occultation Technique. Danish Meteorological Institute Scientific Report 99-6.
- [35] Walters, D., Wood, N., Vosper, S., and Milton, S. (2014). ENDGame: A new dynamical core for seamless atmospheric prediction. Met Office Report. available at [http://www.metoffice.gov.uk/media/pdf/s/h/ENDGameGOVSci\\_v2.0.pdf](http://www.metoffice.gov.uk/media/pdf/s/h/ENDGameGOVSci_v2.0.pdf).
- [36] World Meteorological Organization (2011). Manual on Codes, International Codes, volume I.2.

## A Acronyms and abbreviations

BA	Bending Angle
CDOP-2	Second Continuous Development and Operations Phase
COSMIC	Constellation Observing System for Meteorology, Ionosphere, and Climate
DMI	Danish Meteorological Institute (ROM SAF Leading Entity)
ECMWF	The European Centre for Medium-Range Weather Forecasts
EPS	EUMETSAT Polar Satellite System
EUMETSAT	European Organisation for the Exploitation of Meteorological Satellites
GCOS	Global Climate Observing System
GNSS	Global Navigation Satellite System
GRAS	GNSS Receiver for Atmospheric Sounding (onboard Metop)
GRUAN	GCOS Reference Upper Air Network
IIEC	Institut d'Estudis Espacials de Catalunya
Met Office	United Kingdom Meteorological Office
Metop	Meteorological Operational Polar satellite (EUMETSAT)
NCEP	National Centers for Environmental Prediction
O-B	Observation minus Background
RO	Radio Occultation
ROM SAF	Radio Occultation Meteorology SAF (former GRAS SAF)
ROPP	Radio Occultation Processing Package
RS	Radiosonde
SEA	Solar Elevation Angle
SE	Standard Error
SAF	Satellite Application Facility (EUMETSAT)
SD	Standard Deviation
Tdry	Dry temperature

## B Radiosonde types

**Table B.1:** Extract of the radiosonde types used for TEMP reports submitted to the GTS in 2014 (see World Meteorological Organization [36]). Code 90 that is specified as “unknown, not specified” actually includes three more Russian RS types, namely I-2012, MRZ-3MK, AK2m (Bruce Ingleby, personal communication).

Number	RS type	Produced in
9	No radiosonde - system unknown or not specified	
10	Sippican LMS5	USA
11	Sippican LMS6	USA
14	Vaisala RS92/DigiCORA MW41	Finland
15	PAZA-12M/Radiotheodolite-UL	Ukraine
16	PAZA-22/AVK-1	Ukraine
17	Graw DFM-09	Germany
18	Graw DFM-06	Germany
21	RSG-20A and Jin Yang 1524LA	Korea
22	Meisei RS-11G GPS	Japan
26	Meteolabor SRS-C34/Argus 37	Switzerland
27	AVK-MRZ	Russia
28	AVK -AK2-02	Russia
29	MARL-A and Vektor-M -AK2-02	Russia
30	Meisei RS-06G	Japan
31	Taiyuan GTS1-1/GFE(L)	China
32	Shanghai GTS1-1/GFE(L)	China
33	Nanjing GTS1-2/GFE(L)	China
41	Vaisala RS41 DigiCORA MW41	Finland
49	VIZ MARK II	USA
51	VIZ-B2	USA
52	Vaisala RS92-NGP/Internet IMS-2000	Finland/USA
55	Meisei RS-01G	Japan
57	Modem M2K2-DC	France
58	AVK-BAR	Russia
68	AVK-RZM-2	Russia
69	MARL-A or Vektor-M-RZM-2	Russia
71	Vaisala RS90/Loran/Digicora I, II or Marwin	Finland
75	AVK-MRZ-ARMA	Russia
77	Modem GPSsonde M10	France
78	Vaisala RS90/Digicora III	Finland
79	Vaisala RS92/Digicora I, II or Marwin	Finland
80	Vaisala RS92/Digicora III	Finland
81	Vaisala RS92/Autosonde	Finland
82	Lockheed Martin LMS-6	USA
83	Vaisala RS92-D/Internet IMS 1500	Finland/USA
87	Sippican MARK IIA	USA
88	MARL-A or Vektor-M-MRZ	Russia
89	MARL-A or Vektor-M-BAR	Russia
90	Radiosonde unknown/not specified	
99	Internet	South Africa